


 Cite this: *RSC Adv.*, 2025, **15**, 26321

## Iron oxide nano-adsorbent doped with nickel and palladium for phosphorus removal from water<sup>†</sup>

Pamela Sepúlveda, <sup>ab</sup> Jonathan Suazo-Hernández, <sup>cde</sup> Lizethly Cáceres-Jensen, <sup>f</sup> María de la Luz Mora, <sup>c</sup> Juliano Denardin, <sup>g</sup> Alejandra García-García, <sup>h</sup> Pablo Cornejo <sup>ij</sup> and Binoy Sarkar <sup>ke</sup>

Excessive phosphorus (P) in surface and ground water can cause serious environmental issues. This study aims to synthesize and characterize novel iron oxides ( $Fe_xO_y$ ) nanoparticles (NPs) with and without Ni and Ni–Pd doping and unravel the NPs' performance and mechanism for P removal from water. X-ray diffraction, energy dispersive X-ray spectroscopy and X-ray photoelectron spectroscopy results confirmed successful doping of Ni and Ni–Pd on  $Fe_xO_y$  NPs.  $Fe_xO_y$ –Ni NPs exhibited a higher specific surface area and isoelectric point than  $Fe_xO_y$  and  $Fe_xO_y$ –Ni–Pd NPs. The kinetic data for P adsorption on  $Fe_xO_y$  NPs fitted to the pseudo-first order model and  $Fe_xO_y$ –Ni and  $Fe_xO_y$ –Ni–Pd NPs fitted to the pseudo-second order model. Adsorption isotherm data for  $Fe_xO_y$  NPs fitted to the Freundlich model and  $Fe_xO_y$ –Ni and  $Fe_xO_y$ –Ni–Pd NPs fitted to the Langmuir model. The maximum P adsorption capacity was the highest for  $Fe_xO_y$ –Ni (35.66 mg g<sup>−1</sup>) followed by  $Fe_xO_y$ –Ni–Pd (30.73 mg g<sup>−1</sup>) and  $Fe_xO_y$  NPs (21.97 mg g<sup>−1</sup>), which was opposite to the P desorption order of these adsorbents. The adsorption and characterization analysis suggested that inner-sphere complexes and co-precipitation were the key mechanisms for P adsorption on  $Fe_xO_y$ –Ni and  $Fe_xO_y$ –Ni–Pd NPs. Therefore,  $Fe_xO_y$ –Ni NPs were a highly effective adsorbent for removing P from water.

Received 1st April 2025  
Accepted 9th July 2025

DOI: 10.1039/d5ra02256h  
[rsc.li/rsc-advances](http://rsc.li/rsc-advances)

### 1. Introduction

Phosphorus (P) is an essential element for the development of life on the planet and is widely used in agriculture (fertilizers) and the chemical industry (metal preservatives and detergents).<sup>1</sup> In particular, the application of P fertilizers (e.g., triple superphosphate, diammonium phosphate and phosphate rock) enables P to reach the soil as di-, mono- and tri-hydrogen phosphates ( $H_2PO_4^-$ ,  $HPO_4^{2-}$ , and  $PO_4^{3-}$ ) facilitating plant uptake and optimal plant growth.<sup>2</sup> The volume and number of P fertilizers added to soils have risen in recent decades due to the increased demand for food production resulting from the world population growth.<sup>3</sup> Incremental application volume and improper soil management practices have made plants unable to uptake and utilize all the added P.<sup>4</sup> As a result, P is transported to aquatic systems by surface run-offs and underground water flows,<sup>1,5</sup> accumulating in water bodies and producing freshwater eutrophication.<sup>6</sup> Additional P inputs, especially organic and particulate P species, in water bodies from land application of composts and manures make the eutrophication situation even worse.<sup>7</sup> The eutrophication of water bodies is associated with the formation of harmful algal blooms,<sup>8</sup> putting to disruptions of aquatic ecosystems, which entails serious ecological and economic damage. Due to the serious impact of eutrophication, the United States Environmental Protection Agency (USEPA) has recommended that total P concentration in

<sup>a</sup>Centro de Nanotecnología Aplicada (CNAP), Facultad de Ciencias, Ingeniería y Tecnología, Universidad Mayor, Camino la Pirámide 5750, Huechuraba 8580745, Santiago, Chile

<sup>b</sup>Escuela de Ingeniería en Medio Ambiente y Sustentabilidad, Facultad de Ciencias, Ingeniería y Tecnología, Universidad Mayor, Camino la Pirámide 5750, Huechuraba 8580745, Santiago, Chile

<sup>c</sup>Center of Plant, Soil Interaction and Natural Resources Biotechnology, Scientific and Biotechnological Bioresource Nucleus (BIOREN-UFRO), Universidad de La Frontera, Avenida Francisco Salazar, Temuco 01145, Chile

<sup>d</sup>Facultad de Medicina Veterinaria y Agronomía, Universidad de Las Américas, Sede Concepción, Chile. E-mail: [jsuazo@udla.cl](mailto:jsuazo@udla.cl)

<sup>e</sup>Future Industries Institute, University of South Australia, Mawson Lakes, SA 5095, Australia. E-mail: [binoy.sarkar@unisa.edu.au](mailto:binoy.sarkar@unisa.edu.au)

<sup>f</sup>Physical & Analytical Chemistry Laboratory (PachemLab), Nucleus of Computational Thinking and Education for Sustainable Development (NuCES), Center for Research in Education (CIE-UMCE), Department of Chemistry, Metropolitan University of Educational Sciences, Santiago 776019, Chile

<sup>g</sup>University of Santiago of Chile (USACH), Center for the Development of Nanoscience and Nanotechnology (CEDENNA), Faculty of Science, Physics Department, Avenida Libertador Bernardo O'Higgins, Santiago 3363, Chile

<sup>h</sup>Centro de Investigación en Materiales Avanzados, S.C. (CIMAV), Subsede Monterrey, Av. Alianza Norte 202, Parque PIIT, Apodaca, Nuevo León, CP 66628, Mexico

<sup>i</sup>Centro de Estudios Avanzados en Fruticultura (CEAF), Rengo 2940000, Santiago, Chile

<sup>j</sup>Centro Tecnológico de Suelos y Cultivos (CTSyC), Facultad de Ciencias Agrarias, Universidad de Talca, Talca 3460000, Chile

<sup>†</sup> Electronic supplementary information (ESI) available. See DOI: <https://doi.org/10.1039/d5ra02256h>



lake and dam water should not exceed  $0.01 \text{ mg L}^{-1}$ .<sup>9,10</sup> Whilst the above is an example of a regulatory measure implemented in the USA, eutrophication due to excess P in water has been a global issue in recent years as reports are emerging in many developed and developing countries.<sup>11</sup> Consequently, there is a need to implement methods that can effectively reduce the concentration of P in the aquatic system.

Various simple and complex methods have been used to remove P from aquatic systems, including biological methods and chemical methods such as ion coagulation-sedimentation, exchange, electrochemical methods, and adsorption.<sup>9,12</sup> In particular, adsorption is a low-cost method and reduces concentrations of various contaminants in water systems using adsorbent materials.<sup>13</sup> One key characteristic to consider when using adsorbent materials to remove water contaminants is the amount of contaminant removed by a unit adsorbent mass. This is due to adsorption being a surface reaction because a high specific surface area favors the adsorption capacity of an adsorbent and a high surface area is likely to have a greater number of active sites for adsorption.<sup>14</sup> Additionally, the isoelectric point (IEP) values of adsorbents directly affect the interaction with the contaminants. From IEP, it is possible to establish whether or not there are electrostatic interactions that favor adsorption, or in other words, the adsorption strength.<sup>15</sup>

In this context, studies report that adsorbents of iron oxide ( $\text{Fe}_x\text{O}_y$ ) nanoparticles (NPs) like maghemite ( $\gamma\text{-Fe}_2\text{O}_3$ ), hematite ( $\alpha\text{-Fe}_2\text{O}_3$ ), goethite ( $\alpha\text{-FeOOH}$ ), magnetite ( $\text{Fe}_3\text{O}_4$ ), and feroxylhyte ( $\delta\text{-FeOOH}$ ) are the most suitable materials for water purification and remediation of soil and groundwater contaminated with oxy-anions such as arsenate ( $\text{AsO}_4^{3-}$ ), selenate ( $\text{SeO}_4^{2-}$ ), sulphate ( $\text{SO}_4^{2-}$ ), bicarbonate ( $\text{HCO}_3^-$ ), chromate ( $\text{CrO}_4^{2-}$ ), nitrate ( $\text{NO}_3^-$ ), and especially phosphate ( $\text{PO}_4^{3-}$ ).<sup>16-18</sup> Iron oxide ( $\text{Fe}_x\text{O}_y$ ) NPs are easy to synthesize, non-toxic and inexpensive. In addition, given their high surface area and IEP values (IEP vary between 6 and 9),<sup>19</sup>  $\text{Fe}_x\text{O}_y$  NPs have high selectivity and affinity for phosphates. However, due to their magnetic properties and van der Waals forces, individual  $\text{Fe}_x\text{O}_y$  NPs show easy agglomeration and sedimentation, decreasing their P removal efficiency and preventing their application under natural conditions.<sup>20</sup> As a solution to this problem,  $\text{Fe}_x\text{O}_y$  has been immobilized on inorganic/organic substrates and stabilized with organic molecules and then applied for contaminants removal.<sup>21-23</sup> Furthermore,  $\text{Fe}_x\text{O}_y$  NPs have been doped with metallic elements such as cobalt (Co), nickel (Ni),<sup>24</sup> tin (Sn),<sup>25</sup> manganese (Mn),<sup>26</sup> cerium (Ce),<sup>27</sup> and lanthanum (La)<sup>28</sup> to increase surface area of the adsorbents and improve the adsorption performance. The adsorption performance of such NPs is increased *via* additional electronic transfer between the doped metal(s) present in the structure and the main NPs.<sup>29</sup> Metal doping improves  $\text{Fe}_x\text{O}_y$  NPs performance by enhancing their water stability, colloidal dispersion, oxygen evolution reaction and electrocatalytic activities.<sup>30</sup> As a result of these improvements, doped  $\text{Fe}_x\text{O}_y$  NPs have shown a higher maximum P adsorption capacity ( $q_{\max}$ ) than pure  $\text{Fe}_x\text{O}_y$  NPs. For example, Lai *et al.*<sup>28</sup> reported that  $\text{Fe}_3\text{O}_4\text{-SiO}_2\text{-La}_2\text{O}_3$  had 2.5 times higher  $q_{\max}$  for P than  $\text{Fe}_3\text{O}_4$  NPs. In similar way, Wu *et al.*<sup>31</sup> determined that  $q_{\max}$  of P for  $\text{La(OH)}_3\text{/Fe}_3\text{O}_4$

nanocomposite was 18.6 times higher than for  $\text{Fe}_3\text{O}_4$  NPs. Although there are several studies on the removal of contaminants such as Cr(vi),<sup>32</sup> methylene blue and methyl orange,<sup>33</sup> and As(III)<sup>34</sup> from groundwater, natural water, and wastewater using metal-doped  $\text{Fe}_x\text{O}_y$  NPs, only a few publications to date have reported nutrient, such as P, removal performance of this adsorbent. This study aims to synthesize  $\text{Fe}_x\text{O}_y$  NPs and dope with Ni and Ni-Pd metals, characterize the NPs and determine their P adsorption performances under different experimental conditions. It was hypothesized that  $\text{Fe}_x\text{O}_y$  NPs doped with metals will show a higher surface area than pristine NPs, reduce Fe corrosion from NPs in the aqueous matrix, improve the reactivity of Fe,<sup>35</sup> and in consequence will have a higher adsorption capacity of P than undoped  $\text{Fe}_x\text{O}_y$  NPs. This research will contribute to the knowledge base for developing new nanomaterials to remove P and other contaminants from aqueous systems.

## 2. Materials and methods

### 2.1. Chemicals and reagents

The reagents used in the studies were  $\text{FeCl}_3\cdot 6\text{H}_2\text{O}$  ( $\geq 99\%$  purity),  $\text{FeCl}_2\cdot 4\text{H}_2\text{O}$  (99% purity),  $\text{NiCl}_2\cdot 6\text{H}_2\text{O}$  (99% purity),  $\text{PdCl}_2$  (99% purity),  $\text{NaBH}_4$  (98% purity),  $\text{KH}_2\text{PO}_4$  (99.99% purity),  $\text{NaOH}$  (99.9% purity),  $\text{HCl}$  (99% purity), and  $\text{NaCl}$  ( $\geq 99\%$  purity), all of analytical grade (Merck), and double-distilled and Milli-Q water.

### 2.2. Synthesis of NPs

The NPs were synthesized by chemical reduction of Fe salts with  $\text{NaBH}_4$  as the reducing agent following the methodology proposed by Wang *et al.*<sup>36</sup> with some modifications.<sup>37</sup> The  $\text{Fe}_x\text{O}_y$  NPs were obtained by mixing  $\text{FeCl}_3\cdot 6\text{H}_2\text{O}$  and  $\text{FeCl}_2\cdot 4\text{H}_2\text{O}$  in a 3 : 1 ratio in Milli-Q water. With constant magnetic stirring, 50 mL of ammonia (25%) was added in drops at 80 °C for 60 minutes (min). Next, the black solid was separated from the supernatant by magnetic separation. Finally, the solid obtained was washed with Milli-Q water and dried at 105 °C for 1 hour (h) and then at 60 °C for 24 h. The  $\text{Fe}_x\text{O}_y\text{-Ni}$  NPs were synthesized by mixing the precursor salts of Fe ( $\text{FeCl}_3\cdot 6\text{H}_2\text{O}$  plus  $\text{FeCl}_2\cdot 4\text{H}_2\text{O}$  in a 3 : 1 ratio) and  $\text{NiCl}_2\cdot 6\text{H}_2\text{O}$  in a 1 : 2 ratio in Milli-Q water and stirred for 10 min for homogenization. Then,  $\text{NaBH}_4$  (500 mmol L<sup>-1</sup>) was added dropwise for the reduction reaction to happen over 1 h, after which the solid was separated from the supernatant by magnetic separation. Finally, the solid was washed in Milli-Q water and dried at 105 °C for 1 h and then at 60 °C for 24 h. The  $\text{Fe}_x\text{O}_y\text{-Ni-Pd}$  NPs were synthesized in a method similar to  $\text{Fe}_x\text{O}_y\text{-Ni}$  NPs synthesis where  $\text{PdCl}_2$  was also added as a precursor salt to obtain a Ni :  $\text{Fe}_x\text{O}_y$  : Pd ratio of 1 : 2 : 0.25.

### 2.3. Characterization of NPs

The surface charge of different NPs was determined by measuring the zeta potential (ZP) values using a Nano ZS instrument (Malvern Instruments, Worcestershire, United Kingdom). The NPs (15 mg) were suspended in 10 mL of NaCl



solution (10 mmol L<sup>-1</sup>). The IEP value was obtained from ZP versus pH plots.

The specific surface area (SSA) of NPs was determined by applying the Brunauer–Emmett–Teller (BET) theory and the average pore diameter and pore volume applying the Barrett–Joyner–Halenda (BJH) theory following conducting N<sub>2</sub> adsorption–desorption experiments at liquid N temperature on a Quantachrome Nova 1000e gas sorption analyzer (Boynton Beach, FL, USA). For each ENPs, about 0.5 g of dry powder was outgassed for about 15 h at 150 °C (7 × 10<sup>-6</sup> atm) before performing the measurement.<sup>38</sup>

The morphology and elemental composition of the NPs were visualized using a scanning electron microscope (SEM) Zeiss EVO MA10 (Germany), working at 20 kV and energy-dispersive X-ray spectroscopy (EDS) characterizations were done with an Oxford Aztec Energy with X-act detector. Transmission electron microscope (TEM; Hitachi HT7700, Japan) images were taken with high-resolution and high-contrast visualization configurations. Additionally, NPs were characterized by X-ray diffraction (XRD) using a Bruker D2 Phaser X-ray diffractometer (Germany) equipped with Co K $\alpha$  radiation source. Diffraction patterns were collected at a 2 $\theta$  range of 10–75°. X'Pert HighScore Plus software and TOPAS software were used to analyze the XRD patterns obtained before and after adsorption of P on NPs.

The surface composition of three selected NPs was also examined by X-ray photoelectron spectroscopy (XPS) on a Thermo Fisher Scientific Escalab 250Xi instrument, operated with a conventional Al K $\alpha$  source. Each special region was scanned for three different zones and analyzed using Analyzer 1.20 software. High resolution spectra obtained from O 1s, Fe 2p, Ni 2p, Pd 3d were analyzed.

#### 2.4. Batch adsorption/desorption studies

**2.4.1. Effect of adsorbent dose.** The P (as H<sub>2</sub>PO<sub>4</sub><sup>-</sup>) adsorption capacity of NPs was investigated by batch experiments. To study the effect of the mass of NPs on P adsorption, 20 mL of 200 mg L<sup>-1</sup> P solution<sup>39</sup> at pH 5.5 ± 0.2 (by adding dilute HCl or NaOH) and background electrolyte 10 mmol L<sup>-1</sup> NaCl were added to 50 mL centrifuge tubes varying the NPs mass between 10 and 80 mg. The mixture was then stirred at 200 rpm for 1440 min at 20 ± 2 °C. The tubes were centrifuged at 13 000 rpm using an ultracentrifuge for 12 min and filtered through 0.22 µm syringe filters. The P concentration in the solution was determined using the molybdate blue method on a Rayleigh UV-2601 spectrophotometer (BRAIC Co. Ltd., Beijing, China).<sup>40</sup> The P amount adsorbed ( $q_e$ , mg g<sup>-1</sup>) onto NPs were determined using eqn (1).

$$q_e = (C_0 - C_t)V/w \quad (1)$$

where,  $C_0$  is the initial concentration of P in solution (mg L<sup>-1</sup>),  $C_t$  is the equilibrium concentration of P in solution (mg L<sup>-1</sup>),  $V$  is the volume (L), and  $w$  is the mass (g) of the different NPs used.

**2.4.2. Effect of pH.** The pH effect on P adsorption by different NPs was studied using 50 mg of NPs and 20 mL of 200 mg L<sup>-1</sup> P stock solution of varying the initial pH values between 3.5 ± 0.2 and 10.5 ± 0.2 (by adding dilute HCl or

NaOH) in a background electrolyte of 10 mmol L<sup>-1</sup> NaCl. The mixture was added to 50 mL centrifuge tubes and stirred at 200 rpm for 1440 min at 20 ± 2 °C. The pH was also measured at the end of the experiment (pH<sub>Final</sub>). The tubes were centrifuged at 13 000 rpm for 12 min and the P concentration in the supernatant was determined as previously described.

**2.4.3. Kinetic adsorption.** A kinetic adsorption study was conducted in similar set up as stated earlier with 50 mg of NPs and 200 mg L<sup>-1</sup> P in 10 mmol L<sup>-1</sup> NaCl solution at an initial pH 5.5 ± 0.2 (by adding dilute HCl or NaOH). Samples were withdrawn at time intervals between 0 and 1440 min (0, 2.5, 10, 30, 45, 60, 120, 200, 360, 720 and 1440 min) and analyzed for P concentration in supernatant, as described previously.

**2.4.4. Adsorption isotherm.** Adsorption isotherms were obtained by running experiments with 50 mg of NPs and varying P concentrations between 0.5 and 200 mg L<sup>-1</sup> (ref. 39) in 10 mmol L<sup>-1</sup> NaCl solution at an initial pH 5.5 ± 0.2 (by adding dilute HCl or NaOH). Following stirring, centrifugation, and filtration, as described earlier, the final P concentration in the solution was determined.

**2.4.5. Desorption studies.** To study P desorption from NPs, the first 50 mg of NPs and 20 mL of P solution (200 mg L<sup>-1</sup>) were mixed in 10 mmol L<sup>-1</sup> NaCl solution at an initial pH 5.5 ± 0.2 (by adding dilute HCl or NaOH). The mixture was stirred at 200 rpm for 1440 min at 20 ± 2 °C. The final P concentration in the supernatant solution was determined following stirring, centrifugation and filtration, as described earlier. The residual solution was removed and 20 mL of fresh 10 mmol L<sup>-1</sup> NaCl solution without any P at pH 5.5 ± 0.2 (by adding dilute HCl or NaOH) was added to the solid, and the suspension was stirred, as described above. The desorption cycle was repeated five times. After each desorption cycle, the mixture was centrifuged at 13 000 rpm for 12 min and the P concentration in the supernatant was determined as described previously. The P desorption percentage (%) by NPs after each cycle was calculated using eqn (2).

$$P \text{ desorption (\%)} = (P_{\text{desorbed}}/P_{\text{adsorbed}}) \times 100 \quad (2)$$

where,  $P_{\text{adsorbed}}$  (mg g<sup>-1</sup>) is the amount of P adsorbed by the NPs before NaCl treatment, and  $P_{\text{desorbed}}$  (mg g<sup>-1</sup>) is the amount of P desorbed by the NPs after NaCl treatment.

**2.4.6. Adsorption kinetics and isotherm models.** We tested the experimental kinetic data using the pseudo-second order (PSO), pseudo-first order (PFO), and Elovich equations through non-linear fitting (Table 1SI†). The P adsorption isotherm equilibrium data were tested using the Freundlich and Langmuir equations through non-linear fitting (Table 2SI†).

#### 2.5. Data analysis

All adsorption experiments were done in triplicate, and the results were presented as the mean value. The fitness of experimental data to the kinetic and isotherm models were tested non-linearly using the chi-square ( $\chi^2$ ), coefficient of determination (known as  $R$ -squared,  $r^2$ ), and root mean square error (RMSE) values. The model fitting and figure drawing were done using the Origin 9.0 program.



### 3. Results and discussion

#### 3.1. Characterization of NPs pre- and post-phosphorus adsorption

Fig. 1 shows the SEM and TEM images of the synthesized NPs. Fig. 1a shows the SEM image of  $\text{Fe}_x\text{O}_y$  NPs, suggesting that SEM was unable to delineate the morphological features of these NPs due to their small size and agglomerated nature.<sup>41,42</sup> Nevertheless, the TEM images in Fig. 1d confirmed a pseudo-spherical morphology of the NPs with the formation of agglomerates. An average particle size of 9.6 nm (Feret diameter) was determined for the NPs from the TEM observation. The SEM image in Fig. 1b showed the presence of two areas with different morphology of  $\text{Fe}_x\text{O}_y$ –Ni NPs, which was confirmed in the TEM analysis (Fig. 1e). One of these two areas is related with chains of  $\text{Fe}_x\text{O}_y$  NPs with a Feret diameter of 22.6 nm and the second area is a “sheet” like morphology associated with the formation of NiO (confirmed *via* XRD and EDS Fig. 1a SI†) that coated and maintained the oxidation status of  $\text{Fe}_x\text{O}_y$  NPs. The increase in size of NPs could be attributed to the NiO coating of  $\text{Fe}_x\text{O}_y$  NPs. Finally, for the  $\text{Fe}_x\text{O}_y$ –Ni–Pd NPs, similar to the previously described case, two types of morphology were observed in SEM (Fig. 1c) and TEM (Fig. 1f) images. However, in this case, determination of the average size of NPs was not possible due to the shape and size irregularity and agglomeration of the NPs, which could indicate that  $\text{Fe}_x\text{O}_y$  NPs were likely covered with amorphous layers of PdO and NiO (see EDS, Fig. 1b SI†).<sup>43</sup>

The morphological features of NPs discussed above were corroborated by XRD results (Fig. 2), where identifiable characteristic diffraction peaks of the mineral/compound phases present in the NPs (prior to P adsorption) were observed (Fig. 2a). In the diffraction pattern of  $\text{Fe}_x\text{O}_y$  NPs, the characteristic peaks of  $\text{Fe}_2\text{O}_3$  (ref. code: 00-004-0755) were noted at  $2\theta$  values of  $18.4^\circ$  ( $h, k, l: 111$ ),  $30.2^\circ$  ( $h, k, l: 220$ ),  $35.6^\circ$  ( $h, k, l: 311$ ),  $43.3^\circ$  ( $h, k, l: 321$ ),  $57.3^\circ$  ( $h, k, l: 511$ ), and  $62.8^\circ$  ( $h, k, l: 440$ ).<sup>44</sup> The  $\text{Fe}_x\text{O}_y$ –Ni NPs exhibited a more amorphous phase like diffraction pattern than  $\text{Fe}_x\text{O}_y$  NPs (Fig. 2a). The diffraction peaks were

observed at  $2\theta$  values of  $30.2^\circ$  ( $h, k, l: 220$ ),  $35.5^\circ$  ( $h, k, l: 311$ ),  $43.2^\circ$  ( $h, k, l: 400$ ) and  $62.7^\circ$  ( $h, k, l: 440$ ), associated with  $\text{Fe}_3\text{O}_4$  (ref. code: 01-088-0315).<sup>45</sup> The second and fourth peaks (at  $35.5^\circ$  and  $62.7^\circ$   $2\theta$  above) almost overlapped with characteristic peaks of  $\text{NiFe}_2\text{O}_4$  [ $2\theta = 30.3^\circ$  ( $h, k, l: 220$ ),  $35.6^\circ$  ( $h, k, l: 311$ ),  $44.8^\circ$  ( $h, k, l: 400$ ) and  $63.0^\circ$  ( $h, k, l: 440$ ); ref. code: 01-074-2081]. Finally, for the XRD pattern of  $\text{Fe}_x\text{O}_y$ –Ni–Pd NPs (Fig. 2a), a considerably more amorphous phase like diffractogram than that of  $\text{Fe}_x\text{O}_y$ –Ni NPs was observed, which was consistent with the results of the SEM and TEM analyses (Fig. 1). It was possible to identify diffraction peaks associated with the presence of metallic Pd [ $2\theta = 40.3^\circ$  ( $h, k, l: 111$ ),  $46.8^\circ$  ( $h, k, l: 200$ ), and  $68.4^\circ$  ( $h, k, l: 220$ ) (ref. code: 01-087-0645)].

The XRD patterns of NP samples following P adsorption are shown in Fig. 2b. Irrespective of the NP types, diffraction peaks were observed at  $2\theta$  values of  $35.4^\circ$  ( $h, k, l: 110$ ),  $57.3^\circ$  ( $h, k, l: 018$ ), and  $62.1^\circ$  ( $h, k, l: 214$ ) associated with  $\text{Fe}_2\text{O}_3$  (ref. code: 00-004-0755),<sup>46,47</sup> and at  $2\theta$  values of  $35.5^\circ$  ( $h, k, l: 311$ ),  $57.1^\circ$  ( $h, k, l: 511$ ) and  $62.7^\circ$  ( $h, k, l: 440$ ) associated with  $\text{Fe}_3\text{O}_4$  (ref. code: 01-088-0315).<sup>45</sup> New diffraction peaks suggesting the presence of P-containing phases were identified as  $\text{FePO}_4$  at  $2\theta$  values of  $34.2^\circ$  ( $h, k, l: 200$ ) and  $45.2^\circ$  ( $h, k, l: 202$ ) (ref. code: 00-030-0659), and  $\text{FeFe}_2(\text{PO}_4)_2(\text{OH})_2 \cdot \text{H}_2\text{O}$  at  $2\theta$  values of  $28.1^\circ$  ( $h, k, l: 130$ ),  $31.4^\circ$  ( $h, k, l: 221$ ) and  $31.7^\circ$  ( $h, k, l: 311$ ) (ref. code: 00-026-1138), which demonstrated that adsorption of P on the NPs predominantly occurred at Fe mineral phases.

The characterization using SEM-EDS following P adsorption (Fig. 3) revealed appreciable changes in the morphology of the three NPs and confirmed the presence of P in the NP structure. First, the EDS mapping confirmed the presence of Fe, Ni, and Ni–Pd respectively in  $\text{Fe}_x\text{O}_y$ ,  $\text{Fe}_x\text{O}_y$ –Ni and  $\text{Fe}_x\text{O}_y$ –Ni–Pd along-side other representative elements. The EDS map of  $\text{Fe}_x\text{O}_y$ –P (Fig. 3a and d),  $\text{Fe}_x\text{O}_y$ –Ni–P (Fig. 3b and e) and  $\text{Fe}_x\text{O}_y$ –Ni–Pd–P (Fig. 3c and f) revealed that P was mainly concentrated in the areas with the presence of O and Fe, which was consistent with the XRD results (*i.e.*, through the formation of iron phosphate ( $\text{FePO}_4$ ) phases).

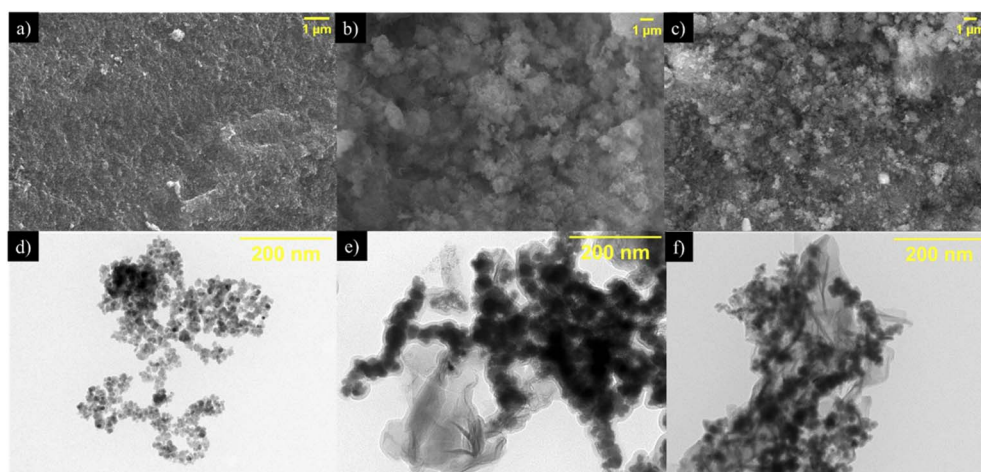


Fig. 1 Scanning electron microscope (a–c) and transmission electron microscope (d–f) micrographs of  $\text{Fe}_x\text{O}_y$  (a and d),  $\text{Fe}_x\text{O}_y$ –Ni (b and e) and  $\text{Fe}_x\text{O}_y$ –Ni–Pd (c and f) nanoparticles.



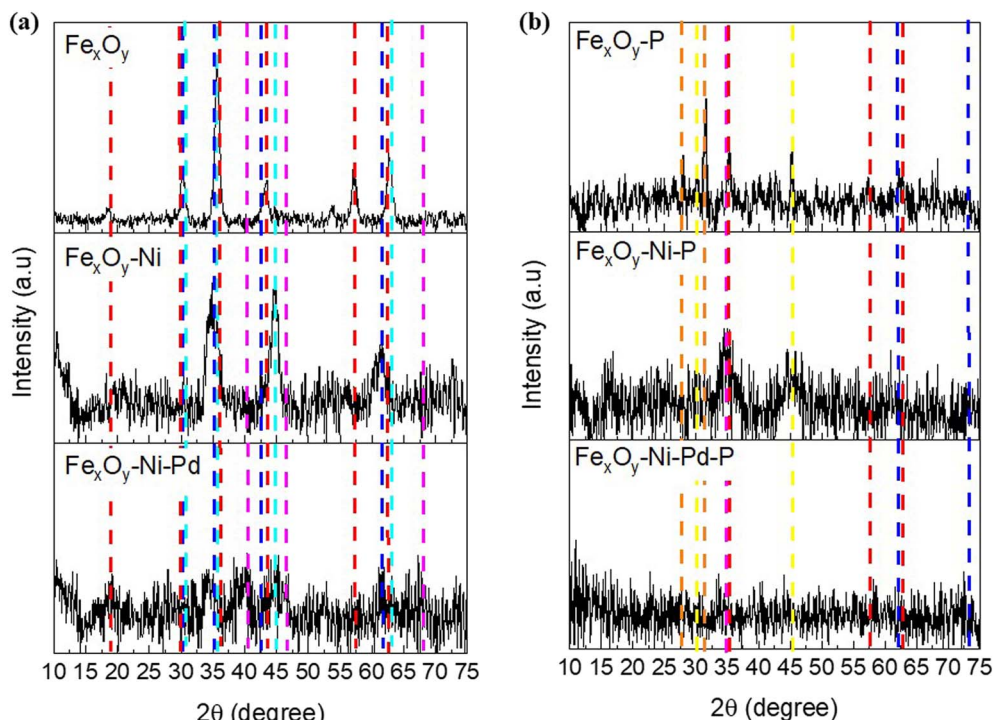


Fig. 2 X-ray diffractograms of  $\text{Fe}_x\text{O}_y$ ,  $\text{Fe}_x\text{O}_y$ -Ni and  $\text{Fe}_x\text{O}_y$ -Ni-Pd nanoparticles (a) before and (b) after adsorption of P. Symbols: —  $\text{Fe}_2\text{O}_3$ , —  $\text{Fe}_3\text{O}_4$ , —  $\text{NiFe}_2\text{O}_4$ , — Pd, —  $\text{FePO}_4$ , —  $\text{FeFe}_2(\text{PO}_4)_2(\text{OH})_2 \cdot \text{H}_2\text{O}$ .

The XPS analysis was conducted to understand the chemical speciation of key elements in the  $\text{Fe}_x\text{O}_y$ ,  $\text{Fe}_x\text{O}_y$ -Ni and  $\text{Fe}_x\text{O}_y$ -Ni-Pd NPs (Fig. 4). In the spectra of  $\text{Fe}_x\text{O}_y$  NPs (Fig. 4a), signals corresponding to iron oxides and oxyhydroxides were identified. Table 1 displays the assigned binding energy values for the different species found, including  $\text{Fe}_2\text{O}_3$  and  $\text{FeOOH}$ , as well as the possibility of existence of  $\text{Fe}_3\text{O}_4$  on the surface of  $\text{Fe}_x\text{O}_y$  NPs. The convolution of the high-resolution O 1s spectrum confirmed the presence of iron oxyhydroxides and oxides (iii).

When Ni was added to  $\text{Fe}_x\text{O}_y$  NPs (Fig. 4b), the surface chemistry of the NPs was changed, as Ni induced changes in the

oxidation states of Fe, stabilizing the NPs.<sup>56</sup> The result was reflected in the species found in the spectra of  $\text{Fe}_x\text{O}_y$ -Ni NPs. In the case of Fe 2p, a peak for  $\text{Fe}^{3+}$  species was observed compared to the spectrum of  $\text{Fe}_2\text{O}_3$  sample. A shift towards higher binding energies (BE) was observed, indicating the interaction of Fe with Ni. These results are consistent with those observed by the XRD analysis results described above and previously published reports. In the Ni 2p spectrum (Fig. 4b), a shift towards higher BE was also observed, indicating an increase in the valence state of Ni due to a synergistic effect between Fe and Ni ions. The oxidation state found for Ni was 3+, indicating the presence of

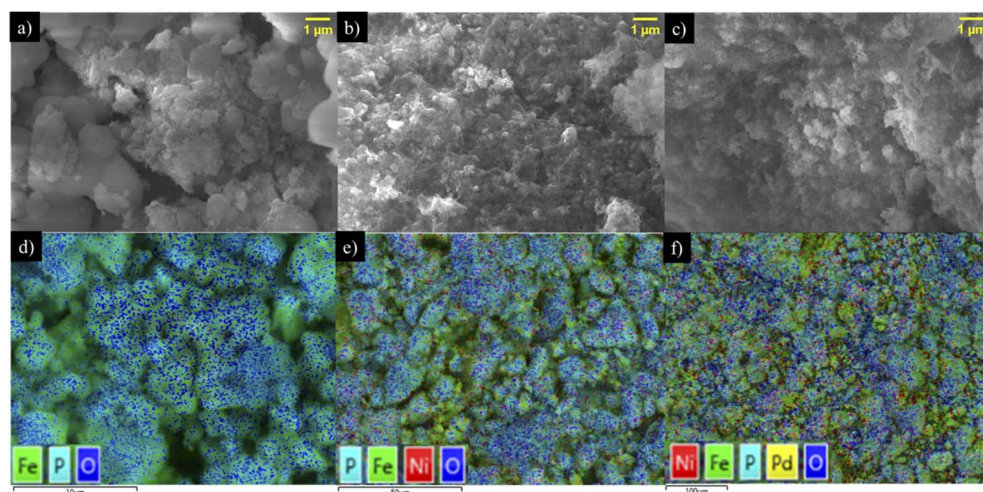


Fig. 3 Scanning electron microscope images (a–c) and energy-dispersive X-ray spectroscopy maps (d–f) of  $\text{Fe}_x\text{O}_y$  (a and d),  $\text{Fe}_x\text{O}_y$ -Ni (b and e) and  $\text{Fe}_x\text{O}_y$ -Ni-Pd (c and f) nanoparticles after adsorption of P.



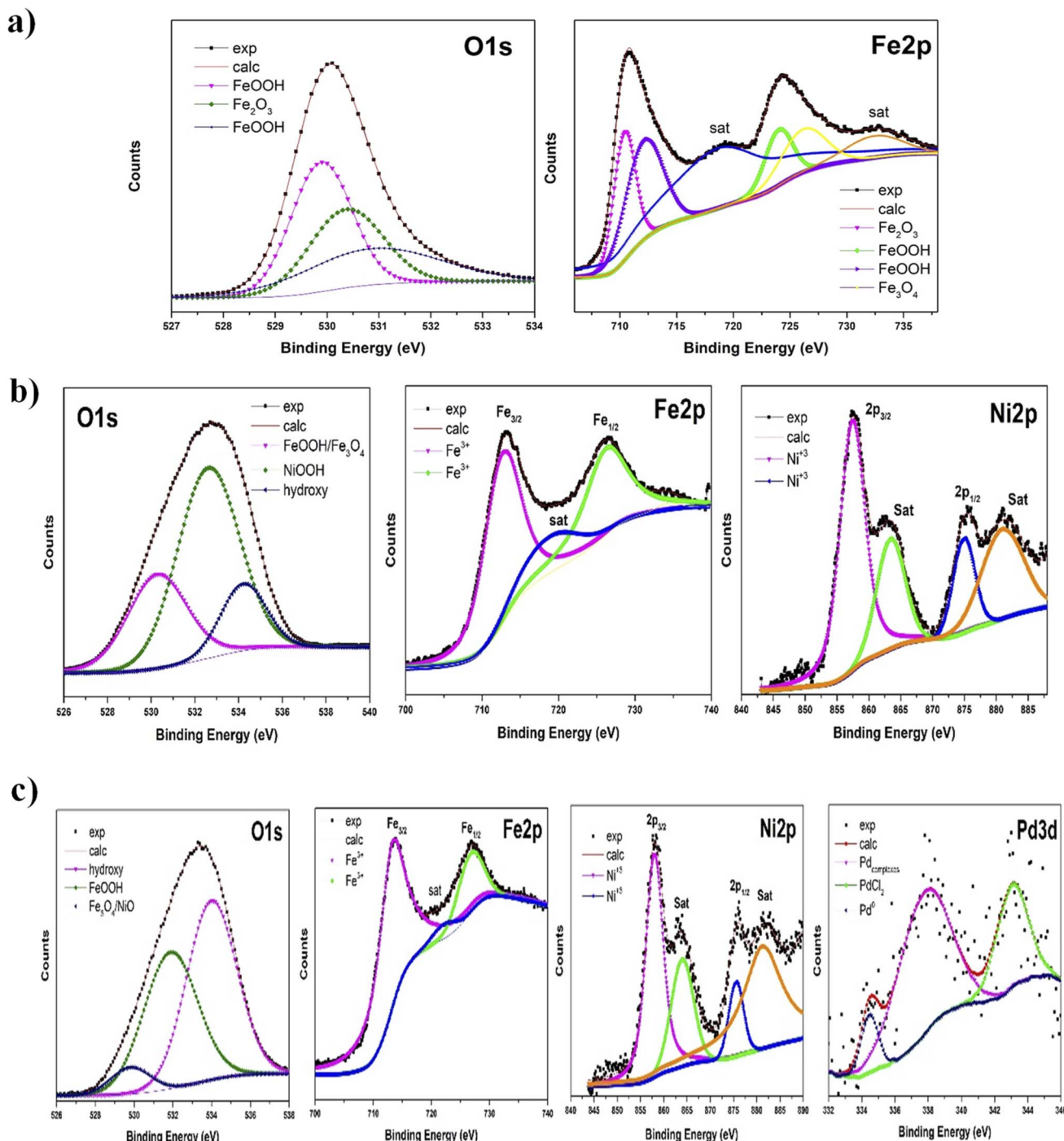


Fig. 4 High resolution XPS spectra of (a) O 1s and Fe 2p for  $\text{Fe}_x\text{O}_y$ , (b) O 1s, Fe 2p and Ni 2p for  $\text{Fe}_x\text{O}_y\text{-Ni}$ , and (c) O 1s, Fe 2p, Ni 2p and Pd 3d for  $\text{Fe}_x\text{O}_y\text{-Ni-Pd}$  nanoparticles.

the chemical species NiOOH, which was also confirmed in the high-resolution O 1s spectrum (Fig. 4b). In this spectrum, the presence of FeOOH on the surface was detected, along with a peak assigned to the -OOH group. However, NiOOH was predominantly available on the surface of this material.

In the case of the  $\text{Fe}_x\text{O}_y\text{-Ni-Pd}$  sample (Fig. 4c), a considerable amount of FeOOH species was found, along with iron oxides such as  $\text{Fe}_2\text{O}_3$  and possibly overlapped Ni oxides, seen in the peak at 529.8 eV in the high-resolution O 1s spectrum.

According to the area under the curve, these oxides' quantity was smaller than iron oxyhydroxides. Only  $\text{Fe}^{3+}$  species were identified for the Fe 2p<sub>3/2</sub> and Fe 2p<sub>1/2</sub> peaks in the high-resolution Fe spectrum. As for Ni, the high-resolution Ni 2p spectrum revealed an oxidation state of 3+ and a shift in the corresponding signals was observed. The shift could be attributed to its interaction with Fe and Pd ions, indicating a change in the electronic nature of Ni. Lastly, in the case of the high-resolution Pd spectrum (Fig. 4c), Pd was found in the zero-



**Table 1** Binding energy values for  $\text{Fe}_x\text{O}_y$ ,  $\text{Fe}_x\text{O}_y\text{-Ni}$  and  $\text{Fe}_x\text{O}_y\text{-Ni-Pd}$  nanoparticles

Level	Binding energy (eV)	Assignment	Reference
<b><math>\text{Fe}_x\text{O}_y</math> NPs</b>			
O 1s	529.9	$\text{Fe}_2\text{O}_3$	48 and 49
	530.1	$\text{FeOOH}$	50
	530.4	$\text{Fe}_3\text{O}_4$	51
	531.1	$\text{FeOOH}$	
Fe 2p	710.5	$\text{Fe}_2\text{O}_3$	52
	712.5	$\text{FeOOH}$	53
	719.2	Sat.	
	724.2	$\text{FeOOH}$	
	726.5	$\text{Fe}_3\text{O}_4$	
	732.8	Sat.	
<b><math>\text{Fe}_x\text{O}_y\text{-Ni}</math> NPs</b>			
O 1s	530.4	$\text{Fe}_2\text{O}_3$	54
	532.7	$\text{NiOOH}$	55
	534.2	-OOH surface hydroxy species	
Ni 2p	857.4	$\text{Ni}^{3+}$ (2p <sub>3/2</sub> )	56
	863.5	Sat.	
	875.2	$\text{Ni}^{3+}$ (2p <sub>1/2</sub> )	
	881.1	Sat.	
Fe 2p	713.0	$\text{Fe}^{3+}$	57
	719.1	Sat.	
	726.5	$\text{Fe}^{3+}$	
<b><math>\text{Fe}_x\text{O}_y\text{-Ni-Pd}</math> NPs</b>			
O 1s	529.8	$\text{Fe}_3\text{O}_4\text{/NiO}$	50
	531.8	$\text{FeOCl/NiCl}$	58
	534.0	-OOH surface hydroxy species	55
Ni 2p	858.0	$\text{Ni}^{3+}$ (2p <sub>3/2</sub> )	56
	864.0	Sat.	
	875.7	$\text{Ni}^{3+}$ (2p <sub>1/2</sub> )	
	881.3	Sat.	
Fe 2p	713.6	$\text{Fe}^{3+}$	59
	722.4	Sat.	
	727.1	$\text{Fe}^{3+}$	
Pd 3d	334.5	Pd	60
	338.0	$\text{PdCl}_4$ (Pd complexes)	
	343.2	$\text{PdCl}_2$	

valent state at a binding energy value of 334.5 eV (the similar form that was identified by XRD technique),<sup>61</sup> along with Pd complexes and probable signals from the initial synthesis precursor. In this composite material, given that the amount of Fe was significantly higher than that of Ni and Pd, it was very likely that Pd and Fe were bonded. However, the presence of some Pd salts indicated that Pd did not react fully, but it affected the Ni species.

### 3.2. Adsorption study

**3.2.1. Effect of adsorbent dose.** Fig. 5 shows the effect of the dose of three NPs on P adsorption. As the dose of the NPs increased, the removal of P increased. When the dose of NPs increased from 10 to 80 mg, the P adsorption varied between 5 and 34% for  $\text{Fe}_x\text{O}_y$  NPs, between 32 and 60% for  $\text{Fe}_x\text{O}_y\text{-Ni}$  NPs and between 23 and 46% for  $\text{Fe}_x\text{O}_y\text{-Ni-Pd}$  NPs. This behavior was attributed to the adsorption of P mediated by the SSA of the NPs (Table 2), where increased SSA created a greater number of

active binding sites on NPs to be occupied by P anions.<sup>62</sup> Fig. 5 also shows that with a mass of NPs greater than 60 mg, a plateau in P adsorption was achieved, which could be explained by the possible overlapping of reactive sites following an excessive increase of the adsorbent mass, thereby reducing the availability of the sites for adsorption. Similar results for P adsorption were obtained using a nano- $\alpha$ - $\text{Fe}_2\text{O}_3$ / $\text{Fe}_3\text{O}_4$ /biochar composite where an adsorbent dose of 50 mg was optimally considered to evaluate P adsorption capacity and rate.<sup>63</sup>

**3.2.2. Effect of pH.** Evaluation of the impact of solution pH on P adsorption was important because an increase in solution pH could (1) influence the dominating P species present in the solution ( $\text{H}_2\text{PO}_4^-$  and  $\text{HPO}_4^{2-}$ ,  $pK_{a2} = 7.2$ ),<sup>64</sup> and increase the ionization of surface functional groups of NPs.<sup>65</sup> Fig. 6a illustrates that when the pH was increased from 3.5 to 10.5, the P adsorption on  $\text{Fe}_x\text{O}_y$  NPs dropped from  $22.98 \text{ mg g}^{-1}$  (28.74%) to  $15.22 \text{ mg g}^{-1}$  (18.90%). This demonstrates that the pH of the solution influenced the adsorption of P by  $\text{Fe}_x\text{O}_y$  NPs. The adsorption at different pH values occurred mainly through inner-sphere complex such as the bidentate phosphate complex.<sup>66</sup> Conversely, an increase in solution pH demonstrated a more prominent effect on P adsorption by  $\text{Fe}_x\text{O}_y\text{-Ni}$  and  $\text{Fe}_x\text{O}_y\text{-Ni-Pd}$  NPs than by  $\text{Fe}_x\text{O}_y$  NPs. For  $\text{Fe}_x\text{O}_y\text{-Ni-Pd}$  NPs, the P adsorption at pH 3.5 was  $32.47 \text{ mg g}^{-1}$  (39.64%), decreasing to  $18.30 \text{ mg g}^{-1}$  (22.75%) at pH 10.5. The P adsorption value for  $\text{Fe}_x\text{O}_y\text{-Ni}$  NPs at pH 3.5 was  $43.53 \text{ mg g}^{-1}$  (54.41%) which decreased to  $22.03 \text{ mg g}^{-1}$  (28.30%) at pH 10.5. These trends were because at a solution pH lower than the IEP of NPs, surface hydroxyl groups became protonated ( $-\text{OH}_2^+$ ) and attracted and adsorbed the negatively charged P anions *via* inner-sphere reaction.<sup>67</sup> Contrarily, at a solution pH higher than the IEP of NPs, P adsorption decreased due to electrostatic repulsion and decreased inner-sphere complex formation.<sup>66</sup>

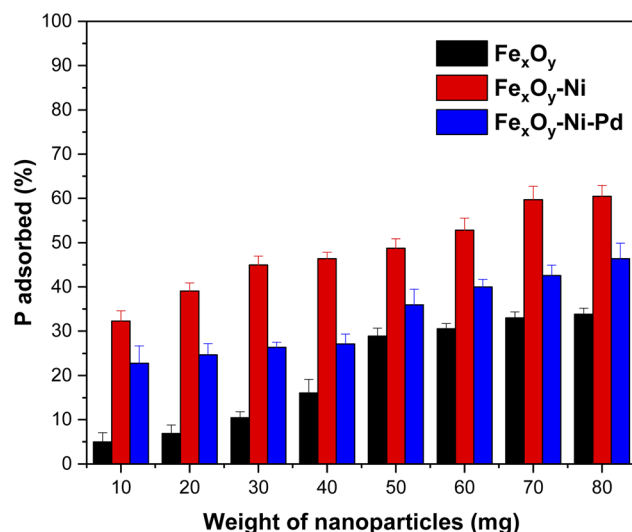


Fig. 5 Effect of adsorbent dose on P adsorption by  $\text{Fe}_x\text{O}_y$ ,  $\text{Fe}_x\text{O}_y\text{-Ni}$ , and  $\text{Fe}_x\text{O}_y\text{-Ni-Pd}$  nanoparticles. Initial P concentration  $200 \text{ mg L}^{-1}$  in  $10 \text{ mmol L}^{-1}$   $\text{NaCl}$ ; initial pH  $5.5 \pm 0.2$ , and reaction volume  $20 \text{ mL}$ . Error bars denote standard deviation;  $n = 3$ .

**Table 2** Specific surface area, pore volume and pore diameter values of nanoparticles (NPs)

NPs	Specific surface area ( $\text{m}^2 \text{ g}^{-1}$ )	Pore volume ( $\text{cm}^3 \text{ g}^{-1}$ )	Pore diameter (nm)
$\text{Fe}_x\text{O}_y$	79.284	0.085	3.814
$\text{Fe}_x\text{O}_y\text{-Ni}$	113.161	0.123	3.777
$\text{Fe}_x\text{O}_y\text{-Ni-Pd}$	98.521	0.098	3.825

Additionally,  $\text{OH}^-$  anions present in the solution at alkaline pH could compete with the P anions, resulting in a low rate of P adsorption by NPs.<sup>67,68</sup> Similar P adsorption trends by iron oxide NPs and iron oxide nanocomposites were previously reported by several researchers.<sup>63,69,70</sup> The change in solution pH ( $\Delta\text{pH} = \text{pH}_{\text{Final}} - \text{pH}_{\text{Initial}}$ ) following P adsorption on NPs supports the above discussion on the adsorption mechanism. The pH change involves the release of  $\text{H}^+$  or  $\text{OH}^-$  from NP surface functional groups and the type of the released ions could indicate the formation of inner- and outer-sphere complexes.<sup>68,71</sup> Fig. 6b shows that after adsorption of P on NPs the values of  $\Delta\text{pH}$  were  $>0$ . In other words,  $\text{OH}^-$  groups were released into the solution, suggesting the formation of inner-sphere complexes between P and the NPs. At  $\text{pH}_{\text{Initial}} 5.5$ , the  $\Delta\text{pH}$  value for the  $\text{Fe}_x\text{O}_y\text{-Ni}$  NPs was 1.41 and 3.70 times higher in relation to  $\text{Fe}_x\text{O}_y\text{-Ni-Pd}$  and  $\text{Fe}_x\text{O}_y$  NPs, respectively, which suggested a higher affinity of  $\text{Fe}_x\text{O}_y\text{-Ni}$  NPs for P than the other two NPs. Therefore, the greater adsorption of P by  $\text{Fe}_x\text{O}_y\text{-Ni}$  NPs compared to  $\text{Fe}_x\text{O}_y\text{-Ni-Pd}$  and  $\text{Fe}_x\text{O}_y$  NPs could be explained by the higher IEP (Fig. 7),  $\Delta\text{pH}$ , and SSA (Table 2) values of  $\text{Fe}_x\text{O}_y\text{-Ni}$  NPs. A possible formation of oxide sheets (could be  $\text{PdO}$ ; see SEM image in Fig. 3f) on  $\text{Fe}_x\text{O}_y\text{-Ni-Pd}$  might have hindered P adsorption to some extent. The type of metal (Ni versus Pd) present in the NPs could also directly affect their affinity for P, as Ogata *et al.*<sup>72</sup> reported that Ni hydroxide showed a high affinity for P.

**3.2.3. Kinetic adsorption.** The adsorption capacity ( $q_e$ ) versus contact time (min) plots for the adsorption of P on NPs (Fig. 8) shows that P concentration in solution decreased rapidly over time. In the first 45 min, the P adsorption capacity was high for  $\text{Fe}_x\text{O}_y$ ,  $\text{Fe}_x\text{O}_y\text{-Ni-Pd}$  and  $\text{Fe}_x\text{O}_y\text{-Ni}$  NPs, amounting to around  $22.2 \text{ mg g}^{-1}$  (27%),  $26.8 \text{ mg g}^{-1}$  (35%) and  $32.4 \text{ mg g}^{-1}$  (41%), respectively. From 60 to 1440 min, the P adsorption capacity was practically constant, reaching a saturation (plateau of the graph) for all three NPs (Fig. 8). At the plateau stage, the adsorption capacity was  $23.6 \text{ mg g}^{-1}$  (31%),  $30.9 \text{ mg g}^{-1}$  (38%), and  $36.2 \text{ mg g}^{-1}$  (46%), respectively, for  $\text{Fe}_x\text{O}_y$ ,  $\text{Fe}_x\text{O}_y\text{-Ni-Pd}$  and  $\text{Fe}_x\text{O}_y\text{-Ni}$  NPs. These results indicated that a long contact time

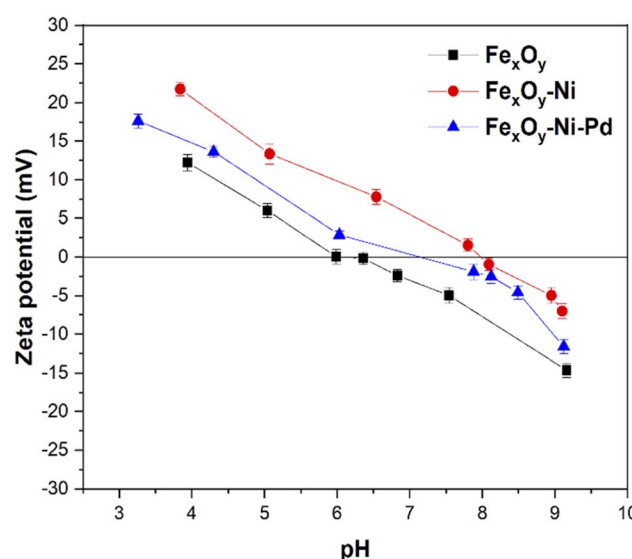


Fig. 7 pH versus zeta potential (mV) curves for  $\text{Fe}_x\text{O}_y$ ,  $\text{Fe}_x\text{O}_y\text{-Ni}$ , and  $\text{Fe}_x\text{O}_y\text{-Ni-Pd}$  nanoparticles. Error bars denote standard deviation;  $n = 3$ .

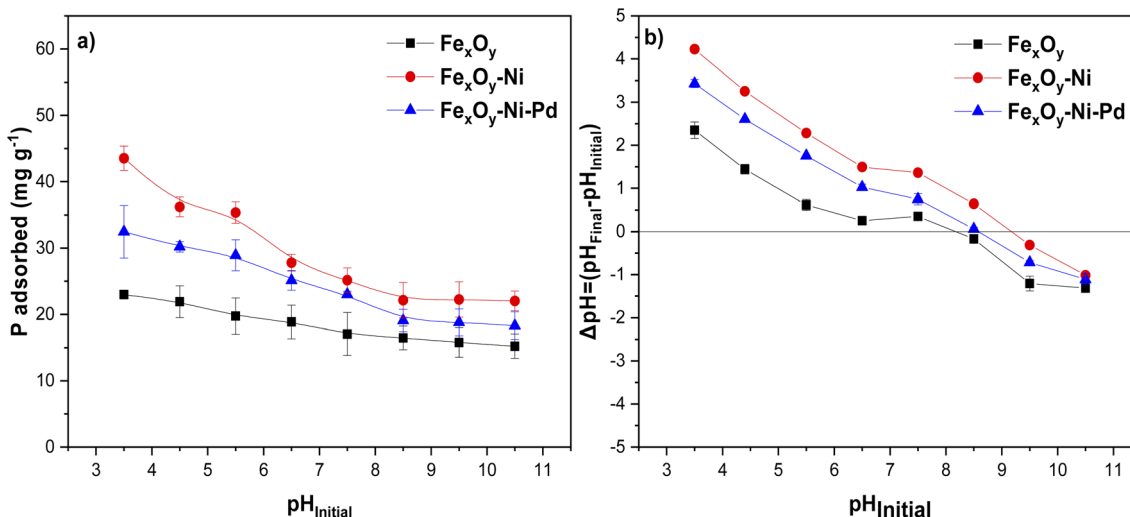


Fig. 6 (a) Effect of initial pH on P adsorption by  $\text{Fe}_x\text{O}_y$ ,  $\text{Fe}_x\text{O}_y\text{-Ni}$ , and  $\text{Fe}_x\text{O}_y\text{-Ni-Pd}$  nanoparticles, and (b) variation of pH ( $\Delta\text{pH}$ ) before and after adsorption at different initial pH values. Initial P concentration  $200 \text{ mg L}^{-1}$  in  $10 \text{ mmol L}^{-1}$  NaCl; initial pH  $5.5 \pm 0.2$ , and reaction volume  $20 \text{ mL}$ . Error bars denote standard deviation;  $n = 3$ .



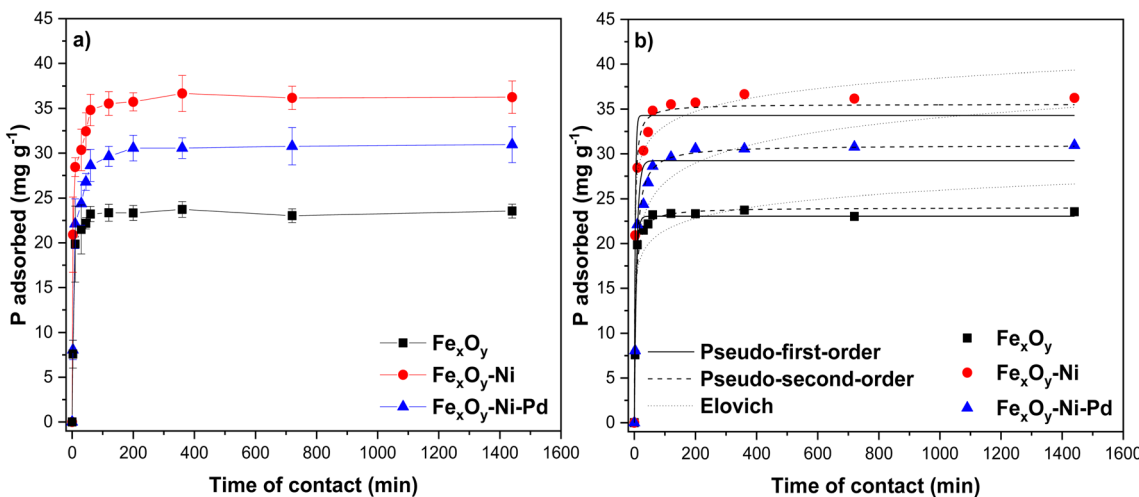


Fig. 8 Kinetics of P adsorption on  $\text{Fe}_x\text{O}_y$ ,  $\text{Fe}_x\text{O}_y$ -Ni, and  $\text{Fe}_x\text{O}_y$ -Ni-Pd nanoparticles (a), and model fitting lines of the experimental data (b). Initial P concentration 200 mg L<sup>-1</sup> in 10 mmol L<sup>-1</sup> NaCl; initial pH 5.5 ± 0.2; reaction volume 20 mL. Error bars denote standard deviation;  $n = 3$ .

would not significantly increase the efficiency of P removal using these NPs. In the first 30 min specifically, the P adsorption rate increased very fast (with a steep slope of the curves) (Fig. 8) due to (1) high attraction forces between P anions and binding sites on NPs and (2) fast diffusion of P anions on NPs to achieve a rapid equilibrium.<sup>73</sup>

The  $q_e$  value for P adsorption by NPs was in the order:  $\text{Fe}_x\text{O}_y$ -Ni >  $\text{Fe}_x\text{O}_y$ -Ni-Pd >  $\text{Fe}_x\text{O}_y$ . This trend could be explained by the smaller particle diameter of  $\text{Fe}_x\text{O}_y$ -Ni than  $\text{Fe}_x\text{O}_y$ -Ni-Pd and  $\text{Fe}_x\text{O}_y$ , as observed in the TEM investigation (Fig. 1b). This led to a larger SSA of  $\text{Fe}_x\text{O}_y$ -Ni than other two NPs (Table 2), and thus presented a greater number of adsorption sites available on the surface for adsorbing P. The incorporation of Pd on the surface of Ni-loaded NPs might have blocked the active sites, diminishing the P adsorption capacity to some extent. Previous research reported that the incorporation of a second or third metal into the structure of NPs could enhance electronic transfer between the metals present in NPs, increasing the reactivity and stability of the adsorbents in an aqueous medium.<sup>74</sup> The present study did not find an increase in P adsorption following incorporation of Pd in  $\text{Fe}_x\text{O}_y$ -Ni; however, whether Pd incorporation affected the stability of the NPs warrants future investigation.

To understand the mechanism of P adsorption on the NPs, the kinetic P adsorption data were tested *via* fitting to the PFO, PSO and Elovich kinetic models. In the case of  $\text{Fe}_x\text{O}_y$  NPs, the  $r^2$  value for PFO model was greater than the PSO model, while the  $\chi^2$ , and RMSE values for PFO model were lower than the obtained for PSO model (Table 3). The low  $\chi^2$  value for the PFO model agreed with the similarity between the  $q_e$  determined from PFO model and that obtained from the experimental data ( $q_{\text{exp}}$ ) (Table 3), suggesting a good fit of the model. This meant that P was bound mainly on the surface of  $\text{Fe}_x\text{O}_y$  NPs forming a monodentate inner-sphere complexes *via* covalent bond interaction,<sup>75</sup> which corroborated with the XRD finding for the possible formation of  $\text{FePO}_4$  (Fig. 2b) following P adsorption. Bhattacharjee *et al.*<sup>76</sup> likewise found that the PFO model

correctly described P adsorption kinetics on nanoscale zero-valent iron. On the other hand, the PSO model for  $\text{Fe}_x\text{O}_y$ -Ni, and  $\text{Fe}_x\text{O}_y$ -Ni-Pd NPs presented higher  $r^2$  values (0.985 and 0.990, respectively) than those obtained from the PFO model. In addition, the  $q_e$  values from the PSO model were closer to the  $q_{\text{exp}}$  than the  $q_e$  values obtained from the PFO model (lower  $\chi^2$  value), and the RMSE values were also lower (Table 3). Therefore, the PSO model showed a better fit of the P adsorption data on  $\text{Fe}_x\text{O}_y$ -Ni and  $\text{Fe}_x\text{O}_y$ -Ni-Pd NPs than PFO model (Table 3). This suggested that P adsorption on  $\text{Fe}_x\text{O}_y$ -Ni and  $\text{Fe}_x\text{O}_y$ -Ni-Pd NPs occurred through a chemical interaction (*i.e.*, inner-sphere complexes) between the adsorption sites and P anions forming a phosphate-iron bidentate complex,<sup>66</sup> which corroborated with the  $\Delta\text{pH}$  data (Fig. 6b), as explained earlier. A good fit to the PSO model also suggested that the P adsorption rate was controlled mainly by the active sites on the surface of  $\text{Fe}_x\text{O}_y$ -Ni NPs, where the adsorption rate was directly proportional to the number of available active sites.<sup>77</sup>

Based on the PSO model, the initial adsorption rate ( $h$ ) value for P adsorption on NPs followed the order:  $\text{Fe}_x\text{O}_y$ -Ni NPs >  $\text{Fe}_x\text{O}_y$  NPs >  $\text{Fe}_x\text{O}_y$ -Ni-Pd NPs (Table 3), which suggested that Ni incorporation to NPs contributed to the generation of new chemical and/or hydrogen (H) surface groups that were available to form bonds with P anions.<sup>78</sup> In addition,  $\text{Fe}_x\text{O}_y$ -Ni NPs showed a  $h$  value higher than the PSO rate constant ( $k_2$ ) (Table 3), indicating that at the initial stage, the available surface sites on  $\text{Fe}_x\text{O}_y$ -Ni NPs were quickly covered by P. Due to the high availability of adsorption sites on  $\text{Fe}_x\text{O}_y$ -Ni NPs, there was an increase in the concentration gradient between P in solution and P in the solid phase (on the adsorbent),<sup>79</sup> which facilitated overall high P adsorption by the Ni-loaded NPs.

A chemisorption process could also be described from the moderate level fitting ( $r^2 = 0.966$ ;  $\chi^2 = 4.498$ ; and RMSE = 2.121) of P adsorption data for  $\text{Fe}_x\text{O}_y$ -Ni NPs to the Elovich model (Table 3), where  $\alpha$  is a constant related with the initial adsorption rate and  $\beta$  with the number of sites available for P adsorption.<sup>80</sup> The surface of  $\text{Fe}_x\text{O}_y$ -Ni NPs showed a high degree



**Table 3** Pseudo-first order, pseudo-second order, and Elovich model parameters for kinetic P adsorption data obtained with  $\text{Fe}_x\text{O}_y$ ,  $\text{Fe}_x\text{O}_y\text{-Ni}$ , and  $\text{Fe}_x\text{O}_y\text{-Ni-Pd}$  nanoparticles (initial P concentration 200 mg L<sup>-1</sup> in 10 mmol L<sup>-1</sup> NaCl; initial pH 5.5 ± 0.2; reaction volume 20 mL)

Kinetic parameters	$\text{Fe}_x\text{O}_y$ NPs	$\text{Fe}_x\text{O}_y\text{-Ni}$ NPs	$\text{Fe}_x\text{O}_y\text{-Ni-Pd}$ NPs
$q_{\text{exp}}$ (mg g <sup>-1</sup> )	23.55 ± 0.78	36.25 ± 1.21	30.95 ± 2.57
$q_{\text{exp}}$ (%)	30.80	45.94	37.59
<b>Pseudo-first-order</b>			
$q_e$ (mg g <sup>-1</sup> )	23.16 ± 0.26	34.30 ± 0.88	29.23 ± 0.70
$k_1$ (×10 <sup>-3</sup> min <sup>-1</sup> )	176.74 ± 14.08	333.16 ± 68.46	127.62 ± 20.73
$r^2$	0.992	0.950	0.969
$\chi^2$	0.523	6.632	3.746
RMSE	0.724	2.575	1.935
<b>Pseudo-second-order</b>			
$q_e$ (mg g <sup>-1</sup> )	24.03 ± 0.46	35.55 ± 0.54	30.98 ± 0.49
$k_2$ (×10 <sup>-3</sup> g mg <sup>-1</sup> min <sup>-1</sup> )	11.18 ± 1.92	13.68 ± 2.18	5.68 ± 0.73
$h$ (mg g <sup>-1</sup> min <sup>-1</sup> )	6.46 ± 0.00	17.29 ± 0.00	5.45 ± 0.00
$r^2$	0.982	0.985	0.990
$\chi^2$	1.241	1.970	1.243
RMSE	1.114	1.403	1.115
<b>Elovich</b>			
$\alpha$ (mg g <sup>-1</sup> min <sup>-1</sup> )	1275.00 ± 91.26	35 990.63 ± 458.01	152.74 ± 17.08
$\beta$ (g mg <sup>-1</sup> )	0.52 ± 0.14	0.43 ± 0.07	0.32 ± 0.06
$r^2$	0.857	0.966	0.899
$\chi^2$	9.892	4.498	12.003
RMSE	3.145	2.121	3.465

of heterogeneity ( $\beta = 0.43 \pm 0.07$  g mg<sup>-1</sup>) with a moderate fitting to the Elovich model (Table 3), which again supported the viability of using  $\text{Fe}_x\text{O}_y\text{-Ni}$  NPs for an efficient P adsorption process.

**3.2.4. Adsorption isotherm.** The plots of  $q_e$  versus  $C_e$  data for P adsorption on the  $\text{Fe}_x\text{O}_y$  NPs followed a L-shape isotherm. In contrast, data of  $\text{Fe}_x\text{O}_y\text{-Ni}$  and  $\text{Fe}_x\text{O}_y\text{-Ni-Pd}$  NPs followed a H-shape isotherm (Fig. 9a). These results indicated that the  $\text{Fe}_x\text{O}_y\text{-Ni}$  and  $\text{Fe}_x\text{O}_y\text{-Ni-Pd}$  NPs had a higher affinity for P than  $\text{Fe}_x\text{O}_y$  NPs. In addition, the H-shape curve showed that a chemisorption mechanism controlled the adsorption of P on  $\text{Fe}_x\text{O}_y\text{-Ni}$  and  $\text{Fe}_x\text{O}_y\text{-Ni-Pd}$  NPs.<sup>81</sup>

The experimental data were fitted to the Langmuir and Freundlich isothermal models to determine the maximum adsorption capacity ( $q_{\text{max}}$ ) and adsorption intensity ( $n$ ).<sup>82</sup> The Freundlich model was able to describe the behavior of P adsorption on  $\text{Fe}_x\text{O}_y$  NPs (Fig. 9b; Table 4), suggesting that the adsorption was a multilayer process on a heterogeneous surface. The Langmuir model particularly presented a better fit to the experimental data of  $\text{Fe}_x\text{O}_y\text{-Ni}$  and  $\text{Fe}_x\text{O}_y\text{-Ni-Pd}$  NPs than the Freundlich model (Table 4). This suggested that P adsorption on  $\text{Fe}_x\text{O}_y\text{-Ni}$  and  $\text{Fe}_x\text{O}_y\text{-Ni-Pd}$  NPs occurred through monolayer interactions on a homogeneous surface.<sup>83</sup> The isotherm results thus conformed with the P adsorption mechanisms (*i.e.*, chemical interactions) on  $\text{Fe}_x\text{O}_y\text{-Ni}$  and  $\text{Fe}_x\text{O}_y\text{-Ni-Pd}$  NPs hypothesized from the kinetic modelling results, as also described previously by Wang *et al.*<sup>84</sup> for P adsorption on  $\text{Fe}^0$ -iron oxide-coated diatomite NPs.

The  $q_{\text{max}}$  value for P adsorption was in the order:  $\text{Fe}_x\text{O}_y\text{-Ni} > \text{Fe}_x\text{O}_y\text{-Ni-Pd} > \text{Fe}_x\text{O}_y$  NPs (Table 4). The  $q_{\text{max}}$  for  $\text{Fe}_x\text{O}_y\text{-Ni}$  NPs

was 1.16 and 1.62 times higher than  $\text{Fe}_x\text{O}_y\text{-Ni-Pd}$  and  $\text{Fe}_x\text{O}_y$  NPs, respectively. These results could be attributed to the physicochemical properties such as larger SSA, pore volume and greater IEP of  $\text{Fe}_x\text{O}_y\text{-Ni}$  than  $\text{Fe}_x\text{O}_y\text{-Ni-Pd}$  and  $\text{Fe}_x\text{O}_y$  NPs (Table 2; Fig. 7). For example,  $\text{Fe}_x\text{O}_y\text{-Ni}$ ,  $\text{Fe}_x\text{O}_y\text{-Ni-Pd}$ , and  $\text{Fe}_x\text{O}_y$  NPs had an IEP value of 7.99, 7.16, and 6.16, respectively (Fig. 7). At a solution pH value of 5.5, the surface of  $\text{Fe}_x\text{O}_y\text{-Ni}$  NPs would have more positive charges than the other two NPs, promoting the adsorption of P anions. High SSA, pore volume and IEP would also contribute to a higher number of active adsorption sites available for P anions on  $\text{Fe}_x\text{O}_y\text{-Ni}$  NPs than  $\text{Fe}_x\text{O}_y\text{-Ni-Pd}$  and  $\text{Fe}_x\text{O}_y$  NPs. The adsorption affinity ( $K_L$ ) values (Table 4) again indicated that the P-binding was more favorable on  $\text{Fe}_x\text{O}_y\text{-Ni}$  NPs than  $\text{Fe}_x\text{O}_y\text{-Ni-Pd}$ , and  $\text{Fe}_x\text{O}_y$  NPs, which was in line with the high affinity of Ni to P previously reported by Ogata *et al.*<sup>72</sup>

Table 5 lists previously reported values of P adsorption capacity (modelled) for a number of  $\text{Fe}_x\text{O}_y$  based materials with a projection for use in P removal from water. The  $\text{Fe}_x\text{O}_y\text{-Ni}$  NPs studied in this research performed better than or at least similar to the previously reported P adsorbents (Table 5), and in consequence these can be useful for the future development of sustainable and practical P removal technologies. The size, morphology, surface charge, SSA, and other surface characteristics of NPs alongside experimental conditions (*e.g.*, pH, and ionic strength) could considerably affect the P adsorption capacity.<sup>85</sup> The current study also demonstrated that incorporating a third metal (Fe–Ni–Pd) in the structure of NPs decreased the P adsorption capacity compared to the bimetallic



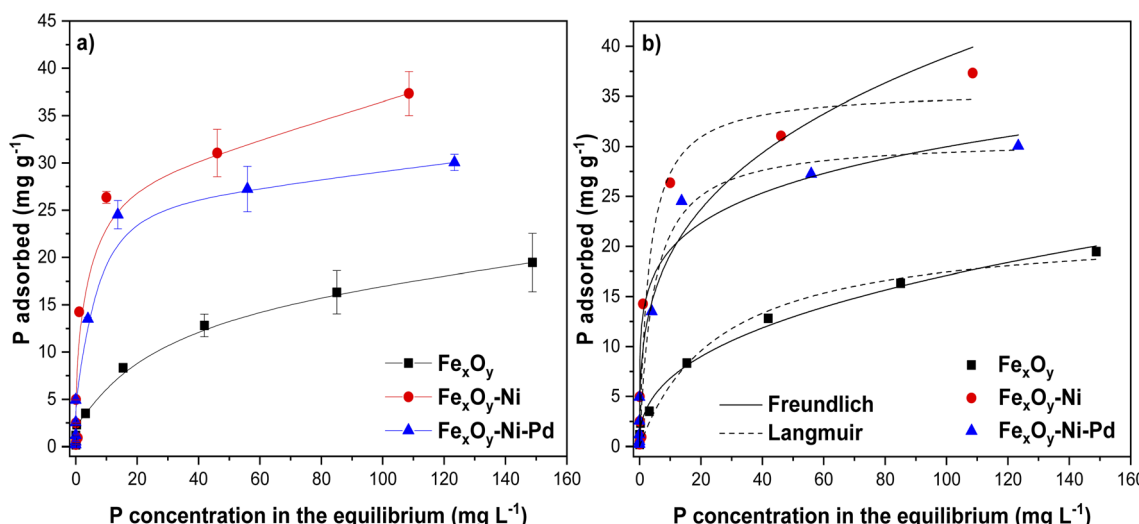


Fig. 9 Isotherms of P adsorption on  $\text{Fe}_x\text{O}_y$ ,  $\text{Fe}_x\text{O}_y\text{-Ni}$ , and  $\text{Fe}_x\text{O}_y\text{-Ni-Pd}$  nanoparticles at an initial pH  $5.5 \pm 0.2$  (a), and (b) model fitting lines of the experimental data. Error bars denote standard deviation;  $n = 3$ .

adsorbent (Fe-Ni) due to chemical changes on the surface of NPs.

#### 4. Desorption study

Desorption of P from the NPs was conducted using a NaCl solution ( $10 \text{ mmol L}^{-1}$ ) as the extracting agent to analyze the cost-effectiveness, reusability, and stability of the NPs synthesized.<sup>92</sup> Fig. 10 shows that after five successive cycles, the desorption of P from  $\text{Fe}_x\text{O}_y$ ,  $\text{Fe}_x\text{O}_y\text{-Ni}$  and  $\text{Fe}_x\text{O}_y\text{-Ni-Pd}$  NPs reached 41.09%, 5.73%, and 27.16%, respectively. The amount of P desorbed from  $\text{Fe}_x\text{O}_y\text{-Ni}$  NPs was 0.14 and 0.21 times lower than  $\text{Fe}_x\text{O}_y$  and  $\text{Fe}_x\text{O}_y\text{-Ni-Pd}$  NPs, respectively. These results are consistent with the  $K_L$  values obtained from the Langmuir isothermal model for the three NPs (Table 4). Moreover, these results reiterated that the presence of Ni helped the  $\text{Fe}_x\text{O}_y$  NPs to form a stronger bond with P than the Pd-Ni mixture, confirming the formation of Fe-P complex for  $\text{Fe}_x\text{O}_y\text{-Ni}$  as identified by XRD analysis (Fig. 2). In terms of easy reusability and

cost-effectiveness for removing anions from water,  $\text{Fe}_x\text{O}_y$  NPs proved to be the most suitable. On the other hand,  $\text{Fe}_x\text{O}_y\text{-Ni}$  NPs would be an ideal candidate for permanently immobilizing an anionic contaminant in water and subsequent recovery from that system due to its magnetic properties.<sup>93</sup>

#### 5. Scalability and applicability challenges

The performance of  $\text{Fe}_x\text{O}_y\text{-Ni}$  NPs in terms of P removal was superior to that of  $\text{Fe}_x\text{O}_y$  NPs, and  $\text{Fe}_x\text{O}_y\text{-Ni-Pd}$  NPs in a laboratory setting. However, further studies are necessary to investigate the scalability and practical application of these NPs and to support their large-scale implementation. At the same time, various issues must be resolved before they can be used. These include the necessity to provide long-term stability, which covers several adsorption/desorption cycles under real water conditions, and the issue of NPs aggregation, which could

Table 4 Langmuir and Freundlich isotherm model parameters for P adsorption on  $\text{Fe}_x\text{O}_y$ ,  $\text{Fe}_x\text{O}_y\text{-Ni}$ , and  $\text{Fe}_x\text{O}_y\text{-Ni-Pd}$  nanoparticles (NPs) at initial pH  $5.5 \pm 0.2$

Isotherm parameters	$\text{Fe}_x\text{O}_y$ NPs	$\text{Fe}_x\text{O}_y\text{-Ni}$ NPs	$\text{Fe}_x\text{O}_y\text{-Ni-Pd}$ NPs
<b>Langmuir</b>			
$K_L$ ( $\text{L mg}^{-1}$ )	$0.04 \pm 0.00$	$0.33 \pm 0.13$	$0.22 \pm 0.07$
$q_{\max}$ ( $\text{mg g}^{-1}$ )	$21.97 \pm 1.65$	$35.66 \pm 2.74$	$30.73 \pm 1.97$
$r^2$	0.981	0.951	0.970
$\chi^2$	1.163	12.07	5.26
RMSE	1.079	3.474	2.233
<b>Freundlich</b>			
$K_F$ ( $\text{mg g}^{-1}(\text{L mg}^{-1})^{1/n}$ )	$2.71 \pm 0.30$	$9.43 \pm 2.13$	$12.98 \pm 2.55$
$n$	$2.51 \pm 0.16$	$3.25 \pm 0.59$	$5.46 \pm 1.50$
$r^2$	0.992	0.908	0.954
$\chi^2$	0.514	22.86	8.12
RMSE	0.717	4.782	2.850

Table 5 Modelled P adsorption capacity values of  $\text{Fe}_x\text{O}_y$  based adsorbent materials

Adsorbents	Model used	Initial pH	Equilibrium time	Maximum adsorption capacity or relative adsorption capacity ( $\text{mg g}^{-1}$ )	Reference
$\text{Fe}_3\text{O}_4$ –diatomite	Langmuir	7.0	60 min	11.89	86
$\text{Fe}_3\text{O}_4$ –illite clay	Langmuir	7.0	60 min	5.48	86
$\text{Fe}^0$ /iron oxide–diatomite	Langmuir	7.0	30 min	37.0	84
$\text{Fe}_2\text{O}_3$ –halloysite nanotubes	Langmuir	4.0	4 h	5.13	87
$\text{La}(\text{OH})_3/\text{Fe}_3\text{O}_4$	Langmuir	7.0	2 h	83.5	31
Iron–carbon nanotubes	Langmuir	—	3 h	36.5	69
Iron(III)–copper(II) binary oxides	Langmuir	7.0	24 h	35.2	88
$\text{Fe}_3\text{O}_4@m\text{ZrO}_2$	Langmuir	3.0	24 h	39.1	23
Zirconium–iron oxide	Freundlich	—	24 h	21.3	89
$\text{Fe}_3\text{O}_4$ – $\text{SiO}_2$ – $\text{La}_2\text{O}_3$	Langmuir	6.6	24 h	27.8	28
Fe–Mn oxide	Langmuir	7.0	24 h	18.4	90
Fe–Zr binary oxide	Langmuir	4.0	24 h	13.65	91
$\text{Fe}_x\text{O}_y$ –Ni–Pd	Langmuir	5.5	24 h	30.73	This study
$\text{Fe}_x\text{O}_y$ –Ni	Langmuir	5.5	24 h	35.66	This study

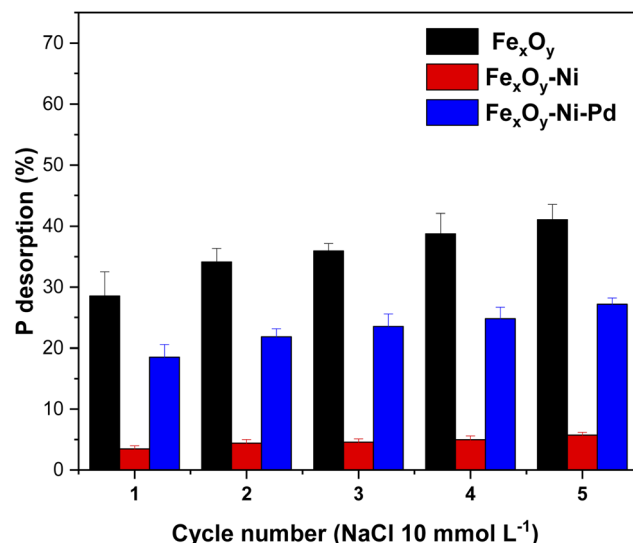


Fig. 10 Desorption (%) of P from  $\text{Fe}_x\text{O}_y$ ,  $\text{Fe}_x\text{O}_y$ –Ni, and  $\text{Fe}_x\text{O}_y$ –Ni–Pd nanoparticles in  $\text{NaCl}$  ( $10 \text{ mmol L}^{-1}$ ) solution over 1440 min at  $20 \pm 2^\circ\text{C}$ . Error bars denote standard deviation;  $n = 3$ .

decrease SSA and consequently their adsorption efficiency. Furthermore, research has shown that the selectivity towards P may be affected in real water systems due to the presence of competing anions, such as  $\text{HCO}_3^-$ ,  $\text{CrO}_4^{2-}$ ,  $\text{AsO}_4^{3-}$ , and  $\text{SO}_4^{2-}$ , and organic matter.<sup>87,94–96</sup>

From an operational perspective, synthesis at an industrial scale and adherence to environmental regulations, particularly concerning the potential leaching of Fe and/or Ni, must also be considered. Therefore, an excellent alternative is to support these NPs on bulk materials or polymer substrates to reduce the Fe leaching process.<sup>97,98</sup> Despite these limitations, the adsorption capacity and magnetic recoverability of these NPs highlight their potential for development into sustainable and effective P adsorption technology, particularly with further optimization and pilot-scale validation.

## 6. Conclusions

This study synthesized, characterized, and tested  $\text{Fe}_x\text{O}_y$  nanoparticles (NPs) with and without Ni and Ni–Pd metal doping as an adsorbent for removing P from water. The maximum phosphorus (P) adsorption capacity ( $q_{\max}$ ) was demonstrated by  $\text{Fe}_x\text{O}_y$ –Ni followed by  $\text{Fe}_x\text{O}_y$ –Ni–Pd, and  $\text{Fe}_x\text{O}_y$  NPs. Contrarily, the desorption of P followed the order:  $\text{Fe}_x\text{O}_y$  >  $\text{Fe}_x\text{O}_y$ –Ni–Pd >  $\text{Fe}_x\text{O}_y$ –Ni NPs. The NPs underwent a surface transformation process, forming new mineralogical phases corresponding to amorphous iron oxides species ( $\text{FePO}_4$  and  $\text{FeFe}_2(\text{PO}_4)_2(\text{OH})_2 \cdot \text{H}_2\text{O}$ ), following the adsorption of P. The P adsorption kinetics for  $\text{Fe}_x\text{O}_y$ –Ni, and  $\text{Fe}_x\text{O}_y$ –Ni–Pd NPs was described by the pseudo-second order model, showing that the P adsorption occurred by inner-sphere bidentate complexes, and for  $\text{Fe}_x\text{O}_y$  NPs, the pseudo-first order model showed a better mathematical fit. The P adsorption on  $\text{Fe}_x\text{O}_y$ –Ni, and  $\text{Fe}_x\text{O}_y$ –Ni–Pd NPs were explained by the Langmuir model, suggesting that the P adsorption occurred by chemisorption. Meanwhile, for  $\text{Fe}_x\text{O}_y$  NPs, the experimental data fitted well to the Freundlich model. Overall, the results suggested that the Ni doping generated an increased specific surface area, and isoelectric point for  $\text{Fe}_x\text{O}_y$  NPs, creating additional sites for P adsorption and enabling inner-sphere complexation and co-precipitation mechanisms on the adsorbent surface. However, doping with Ni–Pd mixture most likely created a PdO coating on  $\text{Fe}_x\text{O}_y$  NPs partially blocking the P adsorption sites, and reducing adsorption affinity. In conclusion, multi-metal oxide nanocomposites— $\text{Fe}_x\text{O}_y$ –Ni NPs was presented as an efficient adsorbent for P removal from polluted water. Future studies should investigate the specific reactions between bi- and tri-metallic NPs and P, long-term stability of NPs, and effect of parameters such as temperature and ionic strength on adsorption performance and use contaminated real wastewater samples. In addition, characterization of NPs using advanced techniques such as X-ray photoelectron spectroscopy and/or transmission electron microscopy-energy dispersive spectroscopy after P adsorption is



necessary to determine the thickness and uniformity of NPs surface layers.

## Data availability

Data will be made available on request.

## Author contributions

Pamela Sepúlveda: conceptualization; funding acquisition; investigation, formal analysis; writing – original draft and review & editing. Jonathan Suazo-Hernández: investigation, formal analysis; methodology; software; conceptualization; visualization; writing – original draft; writing – review & editing. Lizethly Cáceres-Jensen: conceptualization; methodology; visualization; writing – original draft. María de la Luz Mora: conceptualization; funding acquisition. Juliano Denardin: conceptualization; funding acquisition. Alejandra García-García: methodology; resources; supervision, writing – review & editing. Pablo Cornejo: conceptualization; writing – original draft. Binoy Sarkar: conceptualization; supervision; investigation; validation; writing – review & editing.

## Conflicts of interest

The authors declare that there are no conflicts of interest.

## Acknowledgements

Special thanks to Technological Bioresource Nucleus (BIOREN-UFRO) and Soil and Plant Laboratory of Universidad de La Frontera. Pamela Sepúlveda acknowledges ANID-FONDECYT INICIACION No. 11230166. Jonathan Suazo-Hernández acknowledges ANID-FONDECYT/Post-Doctoral Grant No. 3230179. This work was partially funded by the Research Directorate of Universidad de La Frontera.

## References

- 1 X. Zhang, X. Lin, Y. He, Y. Chen, J. Zhou and X. Luo, Adsorption of phosphorus from slaughterhouse wastewater by carboxymethyl konjac glucomannan loaded with lanthanum, *Int. J. Biol. Macromol.*, 2018, **119**, 105–115, DOI: [10.1016/j.ijbiomac.2018.07.140](https://doi.org/10.1016/j.ijbiomac.2018.07.140).
- 2 X. Yu, C. Keitel and F. A. Dijkstra, Global analysis of phosphorus fertilizer use efficiency in cereal crops, *Glob. Food Secur.*, 2021, **29**, 100545, DOI: [10.1016/j.gfs.2021.100545](https://doi.org/10.1016/j.gfs.2021.100545).
- 3 N. B. J. Koning, M. K. Van Ittersum, G. A. Becx, M. A. J. S. Van Boekel, W. A. Brandenburg, J. A. Van den Broek, J. Goudriaan, G. Van Hofwegen, R. A. Jongeneel, J. B. Schiere and M. Smies, Long-term global availability of food: continued abundance or new scarcity, *NJAS – Wagening. J. Life Sci.*, 2008, **55**, 229–292, DOI: [10.1016/S1573-5214\(08\)80001-2](https://doi.org/10.1016/S1573-5214(08)80001-2).
- 4 Y. Zhao, L. Guo, W. Shen, Q. An, Z. Xiao, H. Wang, W. Cai, S. Zhai and Z. L, Function integrated chitosan-based beads with throughout sorption sites and inherent diffusion network for efficient phosphate removal, *Carbohydr. Polym.*, 2020, **230**, 115639, DOI: [10.1016/j.carbpol.2019.115639](https://doi.org/10.1016/j.carbpol.2019.115639).
- 5 K. S. Hashim, H. M. Ewadh, A. A. Muhsin, S. L. Zubaidi, P. Kot, M. Muradov, M. Aljefery and R. Al-Khaddar, Phosphate removal from water using bottom ash: adsorption performance, coexisting anions and modelling studies, *Water Sci. Technol.*, 2021, **83**, 77–89, DOI: [10.2166/wst.2020.561](https://doi.org/10.2166/wst.2020.561).
- 6 E. M. Bennett, S. R. Carpenter and N. F. Caraco, Human impact on erodible phosphorus and eutrophication: a global perspective, *Bioscience*, 2001, **51**, 227–234, DOI: [10.1641/0006-3568\(2001\)051\[0227:HIOEPA\]2.0.CO;2](https://doi.org/10.1641/0006-3568(2001)051[0227:HIOEPA]2.0.CO;2).
- 7 S. Ding, L. Jiao, J. He, L. Li, W. Liu, Y. Liu, Y. Zhu and J. Zheng, Biogeochemical dynamics of particulate organic phosphorus and its potential environmental implication in a typical “algae-type” eutrophic lake, *Environ. Pollut.*, 2022, **314**, 120240, DOI: [10.1016/j.envpol.2022.120240](https://doi.org/10.1016/j.envpol.2022.120240).
- 8 D. M. Anderson, P. M. Glibert and J. M. Burkholder, Harmful algal blooms and eutrophication: nutrient sources, composition, and consequences, *Estuaries*, 2002, **25**, 704–726, DOI: [10.1007/BF02804901](https://doi.org/10.1007/BF02804901).
- 9 P. S. Kumar, L. Korving and M. C. M. Van Loosdrecht, Adsorption as a technology to achieve ultra-low concentrations of phosphate: research gaps and economic analysis, *Water Res.*, 2019, **6**, 100029, DOI: [10.1016/j.wroa.2019.100029](https://doi.org/10.1016/j.wroa.2019.100029).
- 10 G. Gibson, R. Carlson, J. Simpson, E. Smeltzer, J. Gerritsen, S. Chapra, S. Heiskary, J. Jones and R. Kennedy, *Nutrient Criteria Technical Guidance Manual – Lakes and Reservoirs (EPA-822-B-00-001)*, US Gov. Print. Office, Washington, DC, USA, 2000, DOI: [10.7282/t3-6mra-wv76](https://doi.org/10.7282/t3-6mra-wv76).
- 11 G. Fink, J. Alcamo, M. Flörke and K. Reder, Phosphorus Loadings to the World's Largest Lakes: Sources and Trends, *Global Biogeochem. Cycles*, 2018, **32**, 617–634, DOI: [10.1002/2017GB005858](https://doi.org/10.1002/2017GB005858).
- 12 R. Galvez-Cloutier, S. K. M. Saminathan, C. Boillot, G. Triffaut-Bouchet, A. Bourget and G. Soumis-Dugas, An evaluation of several in-lake restoration techniques to improve the water quality problem (eutrophication) of Saint-Augustin Lake, Quebec, Canada, *Environ. Manage.*, 2012, **49**, 1037–1053, DOI: [10.1007/s00267-012-9840-7](https://doi.org/10.1007/s00267-012-9840-7).
- 13 P. S. Thue, M. A. Adebayo, E. C. Lima, J. M. Sieliechi, F. M. Machado, G. L. Dotto, J. C. P. Vaghetti and S. L. P. Dias, Preparation, characterization and application of microwave-assisted activated carbons from wood chips for removal of phenol from aqueous solution, *J. Mol. Liq.*, 2016, **223**, 1067–1080, DOI: [10.1016/j.molliq.2016.09.032](https://doi.org/10.1016/j.molliq.2016.09.032).
- 14 J. Suazo-Hernández, K. Manquián-Cerda, M. de la Luz Mora, M. Molina-Roco, M. Angélica Rubio, B. Sarkar, N. Bolan and N. Arancibia-Miranda, Efficient and selective removal of Se<sup>VI</sup> and As<sup>V</sup> mixed contaminants from aqueous media by montmorillonite-nanoscale zero valent iron nanocomposite, *J. Hazard. Mater.*, 2021, **403**, 123639, DOI: [10.1016/j.jhazmat.2020.123639](https://doi.org/10.1016/j.jhazmat.2020.123639).



15 N. Arancibia-Miranda, J. Silva-Yumi and M. Escudey, Effect of cations in the background electrolyte on the adsorption kinetics of copper and cadmium and the isoelectric point of imogolite, *J. Hazard. Mater.*, 2015, **675–684**, DOI: [10.1016/j.jhazmat.2015.08.007](https://doi.org/10.1016/j.jhazmat.2015.08.007).

16 Z. Pan, X. Zhu, A. Satpathy, W. Li, J. D. Fortner and D. E. Giammar, Cr(VI) Adsorption on Engineered Iron Oxide Nanoparticles: Exploring Complexation Processes and Water Chemistry, *Environ. Sci. Technol.*, 2019, **53**, 11913–11921, DOI: [10.1021/acs.est.9b03796](https://doi.org/10.1021/acs.est.9b03796).

17 Y. Huang, J. K. Yang and A. A. Keller, Removal of arsenic and phosphate from aqueous solution by metal (hydr-)oxide coated sand, *ACS Sustain. Chem. Eng.*, 2014, **2**, 1128–1138, DOI: [10.1021/sc400484s](https://doi.org/10.1021/sc400484s).

18 H. I. Adegoke, F. A. Adekola, O. S. Fatoki and B. J. Ximba, Sorptive interaction of oxyanions with iron oxides: a review, *Pol. J. Environ. Stud.*, 2013, **22**, 7–24.

19 A. F. Schnell, M. Kube and S. Berensmeier, Magnetic Recovery of Cellulase from Cellulose Substrates with Bare Iron Oxide Nanoparticles, *J. Subst. Abuse Treat.*, 1996, **13**, 287–288, DOI: [10.1016/s0740-5472\(96\)90021-5](https://doi.org/10.1016/s0740-5472(96)90021-5).

20 J. Wan, B. Wu and I. M. C. Lo, Development of  $\text{Fe}^0/\text{Fe}_3\text{O}_4$  composites with tunable properties facilitated by  $\text{Fe}^{2+}$  for phosphate removal from river water, *Chem. Eng. J.*, 2020, **388**, 124242, DOI: [10.1016/j.cej.2020.124242](https://doi.org/10.1016/j.cej.2020.124242).

21 L. Bai, X. Su, J. Feng and S. Ma, Preparation of sugarcane bagasse biochar/nano-iron oxide composite and mechanism of its Cr(VI) adsorption in water, *J. Cleaner Prod.*, 2021, **320**, 128723, DOI: [10.1016/j.jclepro.2021.128723](https://doi.org/10.1016/j.jclepro.2021.128723).

22 D. Predoi, S. L. Iconaru, M. V. Predoi and M. Motelica-Heino, Removal and oxidation of As(III) from water using iron oxide coated CTAB as adsorbent, *Polymers*, 2020, **12**, 1687, DOI: [10.3390/POLYM12081687](https://doi.org/10.3390/POLYM12081687).

23 A. Sarkar, S. K. Biswas and P. Pramanik, Design of a new nanostructure comprising mesoporous  $\text{ZrO}_2$  shell and magnetite core ( $\text{Fe}_3\text{O}_4@\text{mZrO}_2$ ) and study of its phosphate ion separation efficiency, *J. Mater. Chem.*, 2010, **20**, 4417–4424, DOI: [10.1039/b925379c](https://doi.org/10.1039/b925379c).

24 W. Chen, Z. Lu, B. Xiao, P. Gu, W. Yao, J. Xing, A. M. Asiri, K. A. Alamry, X. Wang and S. Wang, Enhanced removal of lead ions from aqueous solution by iron oxide nanomaterials with cobalt and nickel doping, *J. Cleaner Prod.*, 2019, **211**, 1250–1258, DOI: [10.1016/j.jclepro.2018.11.254](https://doi.org/10.1016/j.jclepro.2018.11.254).

25 N. Popov, M. Ristić, M. Bošković, M. Perović, S. Musić, D. Stanković and S. Krehula, Influence of Sn doping on the structural, magnetic, optical and photocatalytic properties of hematite ( $\alpha\text{-Fe}_2\text{O}_3$ ) nanoparticles, *J. Phys. Chem. Solids*, 2022, **161**, 110372, DOI: [10.1016/j.jpcs.2021.110372](https://doi.org/10.1016/j.jpcs.2021.110372).

26 H. Su, X. Wang, Y. Sun, D. Xu, L. Li, C. Liu, S. Zeng and D. Sun, Enhancing the Adsorption Capacity of Hematite by Manganese Doping: Facile Synthesis and its Application in the Removal of Congo Red, *Bull. Korean Chem. Soc.*, 2017, **38**, 1155–1162, DOI: [10.1002/bkcs.11239](https://doi.org/10.1002/bkcs.11239).

27 U. K. Sahu, M. K. Sahu, S. S. Mohapatra and R. K. Patel, Removal of As(V) from aqueous solution by Ce-Fe bimetal mixed oxide, *J. Environ. Chem. Eng.*, 2016, **4**, 2892–2899, DOI: [10.1016/j.jece.2016.05.041](https://doi.org/10.1016/j.jece.2016.05.041).

28 L. Lai, Q. Xie, L. Chi, W. Gu and D. Wu, Adsorption of phosphate from water by easily separable  $\text{Fe}_3\text{O}_4@\text{SiO}_2$  core/shell magnetic nanoparticles functionalized with hydrous lanthanum oxide, *J. Colloid Interface Sci.*, 2016, **465**, 76–82, DOI: [10.1016/j.jcis.2015.11.043](https://doi.org/10.1016/j.jcis.2015.11.043).

29 D. O'Carroll, B. Sleep, M. Krol, H. Boparai and C. Kocur, Nanoscale zero valent iron and bimetallic particles for contaminated site remediation, *Adv. Water Resour.*, 2013, **51**, 104–122, DOI: [10.1016/j.advwatres.2012.02.005](https://doi.org/10.1016/j.advwatres.2012.02.005).

30 M. S. Burke, M. G. Kast, L. Trotochaud, A. M. Smith and S. W. Boettcher, Cobalt-Iron (Oxy)hydroxide Oxygen Evolution Electrocatalysts: The Role of Structure and Composition on Activity, Stability, and Mechanism, *J. Am. Chem. Soc.*, 2015, **137**, 3638–3648, DOI: [10.1021/jacs.5b00281](https://doi.org/10.1021/jacs.5b00281).

31 B. Wu, L. Fang, J. D. Fortner, X. Guan and I. M. C. Lo, Highly efficient and selective phosphate removal from wastewater by magnetically recoverable  $\text{La}(\text{OH})_3/\text{Fe}_3\text{O}_4$  nanocomposites, *Water Res.*, 2017, **126**, 179–188, DOI: [10.1016/j.watres.2017.09.034](https://doi.org/10.1016/j.watres.2017.09.034).

32 D. Jiang, D. Huang, C. Lai, P. Xu, G. Zeng, J. Wan, L. Tang, H. Dong, B. Huang and T. Hu, Difunctional chitosan-stabilized Fe/Cu bimetallic nanoparticles for removal of hexavalent chromium wastewater, *Sci. Total Environ.*, 2018, **644**, 1181–1189, DOI: [10.1016/j.scitotenv.2018.06.367](https://doi.org/10.1016/j.scitotenv.2018.06.367).

33 Q. Wu, M. S. Siddique and W. Yu, Iron-nickel bimetallic metal-organic frameworks as bifunctional Fenton-like catalysts for enhanced adsorption and degradation of organic contaminants under visible light: kinetics and mechanistic studies, *J. Hazard. Mater.*, 2021, **401**, 123261, DOI: [10.1016/j.jhazmat.2020.123261](https://doi.org/10.1016/j.jhazmat.2020.123261).

34 Y. Lin, X. Jin, N. I. Khan, G. Owens and Z. Chen, Efficient removal of As(III) by calcined green synthesized bimetallic Fe/Pd nanoparticles based on adsorption and oxidation, *J. Cleaner Prod.*, 2021, **286**, 124987, DOI: [10.1016/j.jclepro.2020.124987](https://doi.org/10.1016/j.jclepro.2020.124987).

35 W. J. Liu, T. T. Qian and H. Jiang, Bimetallic Fe nanoparticles: recent advances in synthesis and application in catalytic elimination of environmental pollutants, *Chem. Eng. J.*, 2014, **236**, 448–463, DOI: [10.1016/j.cej.2013.10.062](https://doi.org/10.1016/j.cej.2013.10.062).

36 C. B. Wang and W. X. Zhang, Synthesizing nanoscale iron particles for rapid and complete dechlorination of TCE and PCBs, *Environ. Sci. Technol.*, 1997, **31**, 2154–2156, DOI: [10.1016/es970039c](https://doi.org/10.1016/es970039c).

37 P. M. Sepúlveda, S. A. Campos, W. Calzadilla, J. F. Marco, J. C. Denardin, P. M. Sepú and R. A. Salazar-González, Pd-Based Nanoparticles as Catalysts for Improved Removal of Florfenicol via Heterogeneous Fenton and Photo-Fenton (-like) Processes, *ACS Appl. Nano Mater.*, 2023, **6**, 12177–12189, DOI: [10.1021/acsanm.3c01915](https://doi.org/10.1021/acsanm.3c01915).

38 L. Macera, V. Daniele, C. Mondelli, M. Capron and G. Taglieri, New sustainable, scalable and one-step synthesis of iron oxide nanoparticles by ion exchange



process, *Nanomaterials*, 2021, **11**, 798, DOI: [10.3390/nano11030798](https://doi.org/10.3390/nano11030798).

39 F. Wu, Q. Yu, F. Gauvin, H. J. H. Brouwers and C. Liu, Phosphorus removal from aqueous solutions by adsorptive concrete aggregates, *J. Cleaner Prod.*, 2021, **278**, 123933, DOI: [10.1016/j.jclepro.2020.123933](https://doi.org/10.1016/j.jclepro.2020.123933).

40 J. Murphy and J. P. Riley, A modified single solution method for the determination of phosphate in natural waters, *Anal. Chim. Acta*, 1962, **27**, 31–36, DOI: [10.1016/S0003-2670\(00\)88444-5](https://doi.org/10.1016/S0003-2670(00)88444-5).

41 T. Mwebembezi, J. Wakatuntu, J. Jjagwe, C. Kanyesigye, R. N. Kulabako and P. W. Olupot, Synthesis, characterization and application of steel waste-based iron oxide nanoparticles for removal of heavy metals from industrial wastewaters, *Helijon*, 2024, **10**, e28153, DOI: [10.1016/j.helijon.2024.e28153](https://doi.org/10.1016/j.helijon.2024.e28153).

42 F. V. Gutierrez, I. S. Lima, A. De Falco, B. M. Ereias, O. Baffa, C. Diego de Abreu Lima, L. I. Moraes Simimbu, P. de la Presa, C. Luz-Lima and J. F. Damasceno Felix Araujo, The effect of temperature on the synthesis of magnetite nanoparticles by the coprecipitation method, *Helijon*, 2024, **10**, e25781, DOI: [10.1016/j.helijon.2024.e25781](https://doi.org/10.1016/j.helijon.2024.e25781).

43 D. A. Petrov, C.-R. Lin, R. D. Ivantsov, S. G. Ovchinnikov, S. M. Zharkov, G. Y. Yurkin, D. A. Velikanov, Y. V. Knyazev, M. S. Molokeev, Y.-T. Tseng, E.-S. Lin, I. S. Edelman, A. O. Baskakov, S. S. Starchikov and I. S. Lyubutin, Characterization of the iron oxide phases formed during the synthesis of core-shell  $\text{Fe}_x\text{O}_y@\text{C}$  nanoparticles modified with Ag, *Nanotechnology*, 2020, **39**, 395703, DOI: [10.1088/1361-6528/ab9af2](https://doi.org/10.1088/1361-6528/ab9af2).

44 F. Mukhtar, T. Munawar, M. S. Nadeem, S. A. Khan, M. Koc, S. Batool, M. Hasan and F. Iqbal, Enhanced sunlight-absorption of  $\text{Fe}_2\text{O}_3$  covered by PANI for the photodegradation of organic pollutants and antimicrobial inactivation, *Adv. Powder Technol.*, 2022, **33**, 103708, DOI: [10.1016/j.apt.2022.103708](https://doi.org/10.1016/j.apt.2022.103708).

45 Y. Y. Zheng, X. B. Wang, L. Shang, C. R. Li, C. Cui, W. J. Dong, W. H. Tang and B. Y. Chen, Fabrication of shape controlled  $\text{Fe}_3\text{O}_4$  nanostructure, *Mater. Charact.*, 2010, **61**, 489–492, DOI: [10.1016/j.matchar.2010.01.008](https://doi.org/10.1016/j.matchar.2010.01.008).

46 R. Al-Gaashani, Y. Zakaria, I. Gladich, V. Kochkodan and J. Lawler, XPS, structural and antimicrobial studies of novel functionalized halloysite nanotubes, *Sci. Rep.*, 2022, **12**, 21633, DOI: [10.1038/s41598-022-25270-7](https://doi.org/10.1038/s41598-022-25270-7).

47 S. Sundar and V. Ganesh, Bio-assisted preparation of efficiently architected nanostructures of  $\gamma\text{-Fe}_2\text{O}_3$  as a molecular recognition platform for simultaneous detection of biomarkers, *Sci. Rep.*, 2020, **10**, 15071, DOI: [10.1038/s41598-020-71934-7](https://doi.org/10.1038/s41598-020-71934-7).

48 D. Brion, Etude par spectroscopie de photoelectrons de la degradation superficielle de  $\text{FeS}_2$ ,  $\text{CuFeS}_2$ ,  $\text{ZnS}$  et  $\text{PbS}$  a l'air et dans l'eau, *Appl. Surf. Sci.*, 1980, **5**, 133–152, DOI: [10.1016/0378-5963\(80\)90148-8](https://doi.org/10.1016/0378-5963(80)90148-8).

49 V. I. Nefedov, D. Gatin, B. F. Dzherinskij, N. P. Sergushin and Y. V. Salyn, X-ray electron investigations of some element oxides, *Zh. Neorg. Khim.*, 1975, **20**, 2307–2314.

50 P. Marcus and J. M. Grimal, The anodic dissolution and passivation of NiCrFe alloys studied by ESCA, *Corros. Sci.*, 1992, **33**, 805–814, DOI: [10.1016/0010-938X\(92\)90113-H](https://doi.org/10.1016/0010-938X(92)90113-H).

51 M. E. Pilleux, C. R. Grahmann and V. M. Fuenzalida, Hydrothermal Strontium Titanate Films on Titanium: An XPS and AES Depth-Profiling Study, *J. Am. Ceram. Soc.*, 1994, **77**, 1601–1604, DOI: [10.1111/j.1151-2916.1994.tb09763.x](https://doi.org/10.1111/j.1151-2916.1994.tb09763.x).

52 O. Havelka, M. Cvek, M. Urbánek, D. Łukowiec, D. Jašiková, M. Kotek, M. Černík, V. Amendola and R. Torres-Mendieta, On the use of laser fragmentation for the synthesis of ligand-free ultra-small iron nanoparticles in various liquid environments, *Nanomaterials*, 2021, **11**, 1538, DOI: [10.3390/nano11061538](https://doi.org/10.3390/nano11061538).

53 Z. Li, X. Tang, K. Liu, J. Huang, Y. Xu, Q. Peng and M. Ao, Synthesis of a  $\text{MnO}_2/\text{Fe}_3\text{O}_4$ /diatomite nanocomposite as an efficient heterogeneous Fenton-like catalyst for methylene blue degradation, *Beilstein J. Nanotechnol.*, 2018, **9**, 1940–1950, DOI: [10.3762/bjnano.9.185](https://doi.org/10.3762/bjnano.9.185).

54 X. Tian, P. Yi, J. Sun, C. Li, R. Liu and J. K. Sun, The Scalable Solid-State Synthesis of a  $\text{Ni}_5\text{P}_4/\text{Ni}_2\text{P}$ -FeNi Alloy Encapsulated into a Hierarchical Porous Carbon Framework for Efficient Oxygen Evolution Reactions, *Nanomaterials*, 2022, **12**, 1848, DOI: [10.3390/nano12111848](https://doi.org/10.3390/nano12111848).

55 Y. Cao, S. Guo, C. Yu, J. Zhang, X. Pan and G. Li, Ionic liquid-assisted one-step preparation of ultrafine amorphous metallic hydroxide nanoparticles for the highly efficient oxygen evolution reaction, *J. Mater. Chem. A*, 2020, **8**, 15767–15773, DOI: [10.1039/d0ta00434k](https://doi.org/10.1039/d0ta00434k).

56 D. Wang, F. Le, J. Lv, X. Yang, X. Chen, H. Yao and W. Jia, Fe-Incorporated Nickel-Based Bimetallic Metal–Organic Frameworks for Enhanced Electrochemical Oxygen Evolution, *Molecules*, 2023, **28**, 4366, DOI: [10.3390/molecules28114366](https://doi.org/10.3390/molecules28114366).

57 W. Yang, Y. Bai, L. Peng, M. Qu and K. Sun, Enhanced oxygen evolution performance of iron-nickel oxide catalyst through dual-defect engineering, *J. Colloid Interface Sci.*, 2023, **648**, 701–708, DOI: [10.1016/j.jcis.2023.05.205](https://doi.org/10.1016/j.jcis.2023.05.205).

58 R. A. Walton, The x-ray photoelectron spectra of metal complexes of sulfur-containing ligands: sulfur 2p binding energies, *Coord. Chem. Rev.*, 1980, **31**, 183–220, DOI: [10.1016/s0010-8545\(00\)80449-x](https://doi.org/10.1016/s0010-8545(00)80449-x).

59 X. Shang, W. Chen, Z. J. Jiang, C. Song and Z. Jiang, In situ growth of  $\text{SeO}_x$  films on the surface of Ni-Fe-selenide nanosheets as highly active and stable electrocatalysts for the oxygen evolution reaction, *Mater. Adv.*, 2022, **3**, 2546–2557, DOI: [10.1039/d1ma01208h](https://doi.org/10.1039/d1ma01208h).

60 Y. Wang, F. F. Shi, Y. Y. Yang and W. Bin Cai, Carbon supported Pd-Ni-P nanoalloy as an efficient catalyst for ethanol electro-oxidation in alkaline media, *J. Power Sources*, 2013, **243**, 369–373, DOI: [10.1016/j.jpowsour.2013.06.021](https://doi.org/10.1016/j.jpowsour.2013.06.021).

61 M. Formenti, M. P. Casaleotto, G. Barone, M. Pagliaro, C. Della Pina, V. Butera and R. Ciriminna, GrafeoPlad Palladium: Insight on Structure and Activity of a New Catalyst Series of Broad Scope, *Adv. Sustainable Syst.*, 2024, 2300643, DOI: [10.1002/adsu.202300643](https://doi.org/10.1002/adsu.202300643).



62 Z. Ajmal, A. Muhamood, M. Usman, S. Kizito, J. Lu, R. Dong and S. Wu, Phosphate removal from aqueous solution using iron oxides: adsorption, desorption and regeneration characteristics, *J. Colloid Interface Sci.*, 2018, **528**, 145–155, DOI: [10.1016/j.jcis.2018.05.084](https://doi.org/10.1016/j.jcis.2018.05.084).

63 Z. Zhu, C. P. Huang, Y. Zhu, W. Wei and H. Qin, A hierarchical porous adsorbent of nano- $\alpha$ -Fe<sub>2</sub>O<sub>3</sub>/Fe<sub>3</sub>O<sub>4</sub> on bamboo biochar (HPA-Fe/C-B) for the removal of phosphate from water, *J. Water Process Eng.*, 2018, **25**, 96–104, DOI: [10.1016/j.jwpe.2018.05.010](https://doi.org/10.1016/j.jwpe.2018.05.010).

64 A. Zhang, S. Fang, H. Xi, J. Huang, Y. Li, G. Ma and J. Zhang, Highly efficient and selective removal of phosphate from wastewater of sea cucumber aquaculture for microalgae culture using a new adsorption-membrane separation-coordinated strategy, *Front. Environ. Sci. Eng.*, 2023, **17**, 120, DOI: [10.1007/s11783-023-1720-2](https://doi.org/10.1007/s11783-023-1720-2).

65 X. Zhang, X. Du, M. Wang, Z. Li, Z. Zhang, C. Tan, J. Liu and H. Li, Stability of SiO<sub>2</sub> nanoparticles with complex environmental conditions with the presence of electrolyte and NOM, *J. Nanopart. Res.*, 2022, **24**, 187, DOI: [10.1007/s11051-022-05555-8](https://doi.org/10.1007/s11051-022-05555-8).

66 L. Hou, Q. Liang and F. Wang, Mechanisms that control the adsorption-desorption behavior of phosphate on magnetite nanoparticles: the role of particle size and surface chemistry characteristics, *RSC Adv.*, 2020, **10**, 2378–2388, DOI: [10.1039/c9ra08517c](https://doi.org/10.1039/c9ra08517c).

67 J. Suazo-Hernández, C. Urdiales, P. Poblete-Grant, H. Pesenti, L. Cáceres-Jensen, B. Sarkar, N. Bolan and M. de la Luz Mora, Effect of particle size of nanoscale zero-valent copper on inorganic phosphorus adsorption-desorption in a volcanic ash soil, *Chemosphere*, 2023, **340**, 139836, DOI: [10.1016/j.chemosphere.2023.139836](https://doi.org/10.1016/j.chemosphere.2023.139836).

68 N. Chen, C. Ni, S. Wu, D. Chen and B. Pan, Enhanced phosphate removal from water by hydrated neodymium oxide-based nanocomposite: performance, mechanism, and validation, *J. Colloid Interface Sci.*, 2023, **633**, 866–875, DOI: [10.1016/j.jcis.2022.11.127](https://doi.org/10.1016/j.jcis.2022.11.127).

69 S. Adil and J. O. Kim, The effectiveness and adsorption mechanism of iron-carbon nanotube composites for removing phosphate from aqueous environments, *Chemosphere*, 2023, **313**, 137629, DOI: [10.1016/j.chemosphere.2022.137629](https://doi.org/10.1016/j.chemosphere.2022.137629).

70 R. Villa-Bellosta and V. Sorribas, Role of rat sodium/phosphate cotransporters in the cell membrane transport of arsenate, *Toxicol. Appl. Pharmacol.*, 2008, **232**, 125–134, DOI: [10.1016/j.taap.2008.05.026](https://doi.org/10.1016/j.taap.2008.05.026).

71 J. Suazo-Hernández, P. Sepúlveda, K. Manquián-Cerda, R. Ramírez-Tagle, M. A. Rubio, N. Bolan, B. Sarkar and N. Arancibia-Miranda, Synthesis and characterization of zeolite-based composites functionalized with nanoscale zero-valent iron for removing arsenic in the presence of selenium from water, *J. Hazard. Mater.*, 2019, **373**, 810–819, DOI: [10.1016/j.jhazmat.2019.03.125](https://doi.org/10.1016/j.jhazmat.2019.03.125).

72 F. Ogata, D. Imai, M. Toda, M. Otani and N. Kawasaki, Properties of a novel adsorbent produced by calcination of nickel hydroxide and its capability for phosphate ion adsorption, *J. Ind. Eng. Chem.*, 2016, **34**, 172–179, DOI: [10.1016/j.jiec.2015.11.005](https://doi.org/10.1016/j.jiec.2015.11.005).

73 A. Ghosh and G. Das, Facile synthesis of Sn(II)-MOF using waste PET bottles as an organic precursor and its derivative SnO<sub>2</sub>NPs: role of surface charge reversal in adsorption of toxic ions, *J. Environ. Chem. Eng.*, 2021, **9**, 105288, DOI: [10.1016/j.jece.2021.105288](https://doi.org/10.1016/j.jece.2021.105288).

74 A. V. B. Reddy, Z. Yusop, J. Jaafar, Y. V. M. Reddy, A. Bin Aris, Z. A. Majid, J. Talib and G. Madhavi, Recent progress on Fe-based nanoparticles: synthesis, properties, characterization and environmental applications, *J. Environ. Chem. Eng.*, 2016, **4**, 3537–3553, DOI: [10.1016/j.jece.2016.07.035](https://doi.org/10.1016/j.jece.2016.07.035).

75 Z. Zhu, H. Zeng, Y. Zhu, F. Yang, H. Zhu, H. Qin and W. Wei, Kinetics and thermodynamic study of phosphate adsorption on the porous biomorph-genetic composite of  $\alpha$ -Fe<sub>2</sub>O<sub>3</sub>/Fe<sub>3</sub>O<sub>4</sub>/C with eucalyptus wood microstructure, *Sep. Purif. Technol.*, 2013, **117**, 124–130, DOI: [10.1016/j.seppur.2013.05.048](https://doi.org/10.1016/j.seppur.2013.05.048).

76 S. Bhattacharjee, N. Darwish and A. Shanableh, Phosphate removal using nanoscale zerovalent iron: impact of chitosan and humic acid, *J. Environ. Chem. Eng.*, 2020, **8**(2020), 104131, DOI: [10.1016/j.jece.2020.104131](https://doi.org/10.1016/j.jece.2020.104131).

77 J. Yang, Z. Wang, R. Li, X. Xu, J. Liu, Y. G. Huang, X. Ye and W. Wang, Effect of Fe(III) Modification on the Phosphorus Removal Behavior of Ce(III) Carbonate Adsorbents, *ACS Omega*, 2022, **7**, 31767–31777, DOI: [10.1021/acsomega.2c02269](https://doi.org/10.1021/acsomega.2c02269).

78 H. Wang, J. Zhu, Q. L. Fu, J. W. Xiong, C. Hong, H. Q. Hu and A. Violante, Adsorption of phosphate onto ferrihydrite and ferrihydrite-humic acid complexes, *Pedosphere*, 2015, **25**, 405–414, DOI: [10.1016/S1002-0160\(15\)30008-4](https://doi.org/10.1016/S1002-0160(15)30008-4).

79 S. Mahdavi, A. Hassani and H. Merrikhpoour, Aqueous phosphorous adsorption onto SnO<sub>2</sub> and WO<sub>3</sub> nanoparticles in batch mode: kinetic, isotherm and thermodynamic study, *J. Exp. Nanosci.*, 2020, **15**, 242–265, DOI: [10.1080/17458080.2020.1770733](https://doi.org/10.1080/17458080.2020.1770733).

80 F. Rassaei, Adsorption Kinetics and Isotherm Modeling of Lead in Calcareous Soils: Insights into Thermodynamics, Desorption, and Soil Properties, *Commun. Soil Sci. Plant Anal.*, 2023, **54**, 2059–2076, DOI: [10.1080/00103624.2023.2211116](https://doi.org/10.1080/00103624.2023.2211116).

81 A. E. Angkawijaya, S. P. Santoso, V. Bundjaja, F. E. Soetaredjo, C. Gunarto, A. Ayucitra, Y. H. Ju, A. W. Go and S. Ismadji, Studies on the performance of bentonite and its composite as phosphate adsorbent and phosphate supplementation for plant, *J. Hazard. Mater.*, 2020, **399**, 123130, DOI: [10.1016/j.jhazmat.2020.123130](https://doi.org/10.1016/j.jhazmat.2020.123130).

82 L. Aljerf, High-efficiency extraction of bromocresol purple dye and heavy metals as chromium from industrial effluent by adsorption onto a modified surface of zeolite: kinetics and equilibrium study, *J. Environ. Manage.*, 2018, **225**, 120–132, DOI: [10.1016/j.jenvman.2018.07.048](https://doi.org/10.1016/j.jenvman.2018.07.048).

83 O. N. Oliveira, L. Caseli and K. Ariga, The Past and the Future of Langmuir and Langmuir-Blodgett Films, *Chem. Rev.*, 2022, **122**, 6459–6513, DOI: [10.1021/acs.chemrev.1c00754](https://doi.org/10.1021/acs.chemrev.1c00754).

84 J. Wang, G. Zhang, S. Qiao and J. Zhou, Magnetic Fe<sup>0</sup>/iron oxide-coated diatomite as a highly efficient adsorbent for



recovering phosphorus from water, *Chem. Eng. J.*, 2021, **412**, 128696, DOI: [10.1016/j.cej.2021.128696](https://doi.org/10.1016/j.cej.2021.128696).

85 J. Suazo-Hernández, P. Sepúlveda, L. Cáceres-Jensen, J. Castro-Rojas, P. Poblete-Grant, N. Bolan and M. d. I. L. Mora, nZVI-Based Nanomaterials Used for Phosphate Removal from Aquatic Systems, *Nanomaterials*, 2023, **13**, 399, DOI: [10.3390/nano13030399](https://doi.org/10.3390/nano13030399).

86 J. Chen, L. Yan, H. Yu, S. Li, L. Qin, G. Liu, Y. Li and B. Du, Efficient removal of phosphate by facile prepared magnetic diatomite and illite clay from aqueous solution, *Chem. Eng. J.*, 2016, **287**, 172, DOI: [10.1039/c6ra16246k](https://doi.org/10.1039/c6ra16246k).

87 D. A. Almasri, N. B. Saleh, M. A. Atieh, G. McKay and S. Ahzi, Adsorption of phosphate on iron oxide doped halloysite nanotubes, *Sci. Rep.*, 2019, **9**, 3232, DOI: [10.1038/s41598-019-39035-2](https://doi.org/10.1038/s41598-019-39035-2).

88 G. Li, S. Gao, G. Zhang and X. Zhang, Enhanced adsorption of phosphate from aqueous solution by nanostructured iron(III)-copper(II) binary oxides, *Chem. Eng. J.*, 2014, **235**, 124–131, DOI: [10.1016/j.cej.2013.09.021](https://doi.org/10.1016/j.cej.2013.09.021).

89 C. Zhang, Y. Li, F. Wang, Z. Yu, J. Wei, Z. Yanga, C. Maa, Z. Lia, Z. Xu and G. Zeng, Performance of magnetic zirconium-iron oxide nanoparticle in the removal of phosphate from aqueous solution, *Appl. Surf. Sci.*, 2017, **396**, 1783–1792, DOI: [10.1016/j.jinf.2020.02.020](https://doi.org/10.1016/j.jinf.2020.02.020).

90 X. Du, Q. Han, J. Li and H. Li, The behavior of phosphate adsorption and its reactions on the surfaces of Fe-Mn oxide adsorbent, *J. Taiwan Inst. Chem. Eng.*, 2017, **76**, 167–175, DOI: [10.1016/j.jtice.2017.04.023](https://doi.org/10.1016/j.jtice.2017.04.023).

91 F. Long, J. L. Gong, G. M. Zeng, L. Chen, X. Y. Wang, J. H. Deng, Q. Y. Niu, H. Y. Zhang and X. R. Zhang, Removal of phosphate from aqueous solution by magnetic Fe-Zr binary oxide, *Chem. Eng. J.*, 2011, **171**, 448–455, DOI: [10.1016/j.cej.2011.03.102](https://doi.org/10.1016/j.cej.2011.03.102).

92 M. A. Rahman, D. Lamb, A. Kunhikrishnan and M. M. Rahman, Kinetics, isotherms and adsorption-desorption behavior of phosphorus from aqueous solution using zirconium-iron and iron modified biosolid biochars, *Water*, 2021, **13**, 3320, DOI: [10.3390/w13233320](https://doi.org/10.3390/w13233320).

93 D. Resende, R. De Jesus, A. Fidelis, M. Pires, S. Domingos, D. Paiva, A. Cesar, G. Filemon, C. Lima and P. Renato, *Journal of Magnetism and Magnetic Materials Magnetite: Properties and Applications – A Review*, *J. Magn. Magn. Mater.*, 2025, **614**, 172770, DOI: [10.1016/j.jmmm.2025.172770](https://doi.org/10.1016/j.jmmm.2025.172770).

94 J. Ren, N. Li, L. Zhao and N. Ren, Enhanced adsorption of phosphate by loading nanosized ferric oxyhydroxide on anion resin, *Front. Environ. Sci. Eng.*, 2014, **8**, 531–538, DOI: [10.1007/s11783-014-0629-1](https://doi.org/10.1007/s11783-014-0629-1).

95 W. H. Lee and J. O. Kim, Effect of coexisting components on phosphate adsorption using magnetite particles in water, *Environ. Sci. Pollut. Res.*, 2019, **26**, 1054–1060, DOI: [10.1007/s11356-017-8528-1](https://doi.org/10.1007/s11356-017-8528-1).

96 M. N. Afridi, W. H. Lee and J. O. Kim, Effect of phosphate concentration, anions, heavy metals, and organic matter on phosphate adsorption from wastewater using anodized iron oxide nanoflakes, *Environ. Res.*, 2019, **171**, 428–436, DOI: [10.1016/j.envres.2019.01.055](https://doi.org/10.1016/j.envres.2019.01.055).

97 J. F. Liu, Z. S. Zhao and G. Bin Jiang, Coating  $\text{Fe}_3\text{O}_4$  magnetic nanoparticles with humic acid for high efficient removal of heavy metals in water, *Environ. Sci. Technol.*, 2008, **42**, 6949–6954, DOI: [10.1021/es800924c](https://doi.org/10.1021/es800924c).

98 M. S. Alam, B. Bishop, N. Chen, S. Safari, V. Warter, J. M. Byrne, T. Warchola, A. Kappler, K. O. Konhauser and D. S. Alessi, Reusable magnetite nanoparticles–biochar composites for the efficient removal of chromate from water, *Sci. Rep.*, 2020, **10**, 1–12, DOI: [10.1038/s41598-020-75924-7](https://doi.org/10.1038/s41598-020-75924-7).

